Redox Biology 81 (2025) 103556

Contents lists available at ScienceDirect

Redox Biology

journal homepage: www.elsevier.com/locate/redox

Mesenchymal stem cell-derived extracellular vesicles attenuate ferroptosis in aged hepatic ischemia/reperfusion injury by transferring miR-1275

Yihang Gong [a,b,1], Qiang You [a,b,1], Xiaofeng Yuan [c,1], Fanxin Zeng [a,b,1], Feng Zhang [d], Jiaqi Xiao [a,b], Haitian Chen [a,b], Yasong Liu [a,b], Tingting Wang [a,b], Xijing Yan [e], Wenjie Chen [d], Yingcai Zhang [a,b], Qi Zhang [d], Jia Yao [a,b], Jiebin Zhang [a,b,*], Rong Li [b,**], Jun Zheng [a,b,***]

[a] Department of Hepatic Surgery and Liver Transplantation Center of the Third Affiliated Hospital of Sun Yat-sen University, Organ Transplantation Research Center of Guangdong Province, Guangdong Province Engineering Laboratory for Transplantation Medicine, Guangzhou, 510630, China
[b] Guangdong Provincial Key Laboratory of Liver Disease Research, Third Affiliated Hospital of Sun Yat-sen University, Guangzhou, 510630, China
[c] Department of General Intensive Care Unit, Lingnan Hospital, The Third Affiliated Hospital of Sun Yat-sen University, Guangzhou, 510530, China
[d] Biological Treatment Center, The Third Affiliated Hospital of Sun Yat-sen University, Guangzhou, 510530, China
[e] Department of Breast and Thyroid Surgery, Lingnan Hospital, The Third Affiliated Hospital of Sun Yat-sen University, Guangzhou, 510530, China

ARTICLE INFO

Keywords:
Old liver
Ischemia/reperfusion injury
Ferroptosis
MSC-EVs
SLC39A14

ABSTRACT

With an aging global population, the proportion of aged donor livers in graft pools is steadily increasing. Compared to young livers, aged livers exhibit heightened susceptibility to hepatic ischemia/reperfusion injury (HIRI), which significantly limits their utilisation in liver transplantation (LT) and exacerbates organ shortages. Our previous study demonstrated that ferroptosis is a pivotal trigger for HIRI vulnerability in aged livers. However, effective clinical strategies for the inhibition of ferroptosis remain elusive. Utilizing an aged mouse HIRI model, primary hepatocytes, and human liver organoids, this study provides hitherto undocumented evidence that mesenchymal stem cell-derived extracellular vesicles (MSC-EVs) effectively alleviate HIRI in aged livers by inhibiting ferroptosis. Mechanistically, miR-1275, which was significantly enriched within MSC-EVs, was transferred to hepatocytes. Subsequently, miR-1275 downregulated the expression of SLC39A14, a crucial iron transporter that is upregulated in aged livers and plays a pivotal role in promoting ferroptosis. Furthermore, we found a negative correlation between SLC39A14 levels and prognosis of aged donor liver recipients using clinical LT samples. Silencing miR-1275 in MSC-EVs or modulating SLC39A14 levels in aged livers reversed MSC-EV-mediated mitigation of ferroptosis. Collectively, these findings revealed the novel therapeutic potential of MSC-EVs in attenuating aged HIRI, suggesting a promising treatment for improving prognosis and preventing serious complications in recipients of aged liver grafts during LT.

1. Introduction

Liver transplantation (LT) is the most effective treatment for end-stage liver diseases. However, the imbalance between graft demand and supply seriously hinders the practice of LT, which promotes the utilisation of "marginal donors" (those extending donor criteria). With the aging population becoming a global challenge, aged donor livers are being utilized and are gradually becoming a critical source of marginal grafts [1,2]. Aging does not significantly influence liver function under normal physiological conditions. However, aged livers are now known to be more susceptible to external stress than young livers. During transplantation, aged donor livers are particularly vulnerable to hepatic

* Corresponding author. Department of Hepatic Surgery and Liver Transplantation Center, the Third Affiliated Hospital of Sun Yat-sen University; Organ Transplantation Research Center of Guangdong Province. Guangzhou, Guangdong Province 510630, China.
** Corresponding author.
*** Corresponding author. Department of Hepatic Surgery and Liver Transplantation Center, the Third Affiliated Hospital of Sun Yat-sen University; Organ Transplantation Research Center of Guangdong Province. Guangzhou, Guangdong Province 510630, China.
E-mail addresses: zhjieb@mail2.sysu.edu.cn (J. Zhang), lirong53@mail.sysu.edu.cn (R. Li), zhengj67@mail2.sysu.edu.cn (J. Zheng).
[1] These authors contributed equally to this work.

https://doi.org/10.1016/j.redox.2025.103556
Received 20 January 2025; Received in revised form 10 February 2025; Accepted 17 February 2025
Available online 18 February 2025

ischemia/reperfusion injury (HIRI), predisposing them to early allograft dysfunction and failure, limiting their utilisation in LT [3]. Despite recent advancements, the underlying mechanisms of age-related HIRI remain unclear. Furthermore, effective clinical treatments to alleviate ischemia/reperfusion injury (IRI) in the aged liver are still lacking.

Ferroptosis is a novel mechanism of cell death, characterized by iron accumulation and lipid peroxidation (iron-mediated phospholipid peroxidation) [4,5]. Given that the liver is a critical organ for iron storage, ferroptosis has been shown to participate in various liver diseases, such as HIRI [4–8]. Yamada was the first to report the involvement of ferroptosis in the pathogenesis of HIRI [9]. Several mechanisms underlying ferroptosis in HIRI have been reported. The ubiquitin ligase E3 HUWE1/MULE inhibits ferroptosis during HIRI by degrading transferrin receptor protein 1 (TFRC) [10]. Furthermore, transmembrane member 16A (TMEM16A) can lead to the degradation of glutathione peroxidase 4 (GPX4), aggravating HIRI [11]. Given that aged livers exhibit increased lipid disorders and iron ion accumulation, our recent study demonstrated the role of ferroptosis in aged HIRI. We found that downregulation of fat mass and obesity-associated genes (*FTO*) in aged livers enhanced the stability of acyl-CoA synthetase long-chain family 4 (ACSL4) and TFRC at the mRNA level, which further induced ferroptosis in aged livers and aggravated HIRI [12]. Therefore, approaches targeting ferroptosis may offer potential therapeutic strategies for mitigating HIRI and improving the prognosis of recipients undergoing LT with aged donor livers.

With their promising potential for immunomodulation and the promotion of tissue repair and regeneration, mesenchymal stem cells (MSCs) have gradually been identified as an effective treatment for liver diseases. Previously, our research group demonstrated that MSCs can attenuate HIRI and have a clinical translation potential for preventing and curing serious complications after LT [13–17]. Multiple lines of evidence have demonstrated that extracellular vesicles (EVs), 30–300 nm in diameter are the primary mode by which MSCs exert their biological functions. These EVs have abundant functional content. As nanosized vesicles, mesenchymal stem cell-derived extracellular vesicles (MSC-EVs) exhibit a therapeutic potential similar to their parent MSCs and possess unique advantages, including high safety and low rates of tumorigenicity and embolism [18]. Our previous study demonstrated the immunoregulatory capacity of MSC-EVs and reduced oxidative stress, which contributed to the attenuation of HIRI [19–22]. In a recent study, we reported that MSC-EVs could promote aged liver regeneration by restoring mitochondrial function in aged hepatocytes [23]. Other studies have also reported the roles of MSC-EVs in inhibiting ferroptosis to improve pathological damage in several diseases, such as abdominal aortic aneurysm, inflammatory bowel disease, and acute spinal cord injury [24–26]. However, whether MSC-EVs can be used to mitigate HIRI in recipients undergoing LT with aged donor livers and the underlying mechanisms remain largely unknown.

In this study, we demonstrated for the first time that MSC-EVs could alleviate age-related HIRI by inhibiting ferroptosis. Mechanistically, MSC-EVs transferred miR-1275 into aged hepatocytes. This miRNA inhibits the expression of the iron transporter SLC39A14, subsequently limiting iron ion accumulation, and ultimately suppressing ferroptosis. We further validated this hypothesis using MSC-EVs in combination with miR-1275 inhibitors. In summary, these data highlight, for the first time in our knowledge, the potential of MSC-EVs in protecting aged donor livers.

2. Methods and materials

2.1. Isolation and identification of MSCs derived from umbilical cords (UCs)

The procedure for isolating MSCs was approved by the Research Ethics Committee of the Third Affiliated Hospital of Sun Yat-sen University and conducted under sterile conditions following standardized protocols [20]. After obtaining informed consent from parturients, UCs were acquired and transferred to the laboratory. UCs were subsequently washed with 4 °C phosphate-buffered saline (PBS) to remove residual blood. The samples were then cut into 10 mm^3 pieces, digested in type I collagenase with $CaCl_2$ (3 mM) and hyaluronidase (0.1 %) for 4 h at 37 °C, and then incubated in low-glucose Dulbecco's Modified Eagle's Medium (DMEM, 1 g/L, Gibco, Life Technologies, NY, USA) supplemented with 10 % fetal bovine serum (FBS, PAN-Biotech, Germany) in a humidified atmosphere containing 5 % CO_2 at 37 °C. The culture medium was changed every three days to remove non-adherent cells.

To investigate MSC-related surface markers, cells were incubated for 30 min at 4 °C in the dark with monoclonal antibodies, including FITC-conjugated CD90, PE-conjugated CD73, FITC-conjugated CD19, FITC-conjugated CD11b, FITC-conjugated CD45, PE-conjugated CD105, FITC-conjugated CD34, and FITC-conjugated HLA-DR. The fluorescence intensity of the stained cells was measured using a thirteen-color FACS Calibur flow cytometer (Beckman Coulter, Hercules, CA, USA) and analyzed with FlowJo software (Tree Star, San Carlos, CA, USA).

To investigate the ability of osteogenic and adipogenic differentiation, the cells were cultured in media specifically designed for adipogenesis and osteogenesis (Gibco, Life Technologies, NY, USA). After twenty-one days, the samples were respectively treated with Alizarin Red S or Oil Red O.

2.2. Purification and identification of MSC-EVs

When cell confluence reached 70–80 %, the culture medium was replaced with 1 g/L glucose DMEM supplemented with 10 % exosome-free FBS. After 48 h, the cell culture medium was harvested and subjected to centrifugation at 3200×*g* for 10 min at 4 °C to remove residual cells. Subsequently, the samples were subjected to ultracentrifugation at 10,000×*g* for 30 min at 4 °C to discard cellular debris, followed by two sequential ultracentrifugation steps at 100,000×*g* for 2 h at 4 °C to purify MSC-EVs (Fig. 1A). The total protein content of the isolated MSC-EVs was quantified using a bicinchoninic acid (BCA) protein assay kit (KeyGEN BioTECH, Jiangsu, China) according to the manufacturer's instructions.

Transmission electron microscopy (TEM) was performed to directly investigate MSC-EVs, as previously described [27]. Following fixation with 2.5 % glutaraldehyde at 4 °C for 1 h, samples were adsorbed onto formvar/carbon-coated grids, negatively stained with 3 % aqueous phosphotungstic acid, and examined using TEM. Nanoparticle tracking analysis (NTA) was conducted using a ZetaView PMX 120 (Particle Metrix, Germany) equipped with an sCMOS camera. Data were analyzed using NTA software (ZetaView, version 8.05.14.SP7) to determine MSC-EV size distribution.

2.3. Clinical data and liver specimen collection

This study was approved by the Ethics Committee of the Third Affiliated Hospital of Sun Yat-sen University (Guangzhou, China), and informed consent was obtained from all participants. Paired liver specimens from donors of varying ages were collected during two phases of orthotopic liver transplantation (OLT)—ischemia and reperfusion—at the Department of Hepatic Surgery and Liver Transplantation Center of the Third Affiliated Hospital of Sun Yat-sen University between May 2020 and November 2021. Ischemic grafts were harvested within 3 h of cold perfusion, and reperfusion tissue samples were obtained within 2 h of hepatic artery anastomosis. Serum alanine aminotransferase (ALT) and aspartate aminotransferase (AST) levels were recorded for the corresponding recipients from postoperative day 1 (POD1) to POD7.

2.4. Animals

All experimental animals used in this study were C57BL/6 mice. Aged mice (20–24 months) and young mice (2 months) were obtained

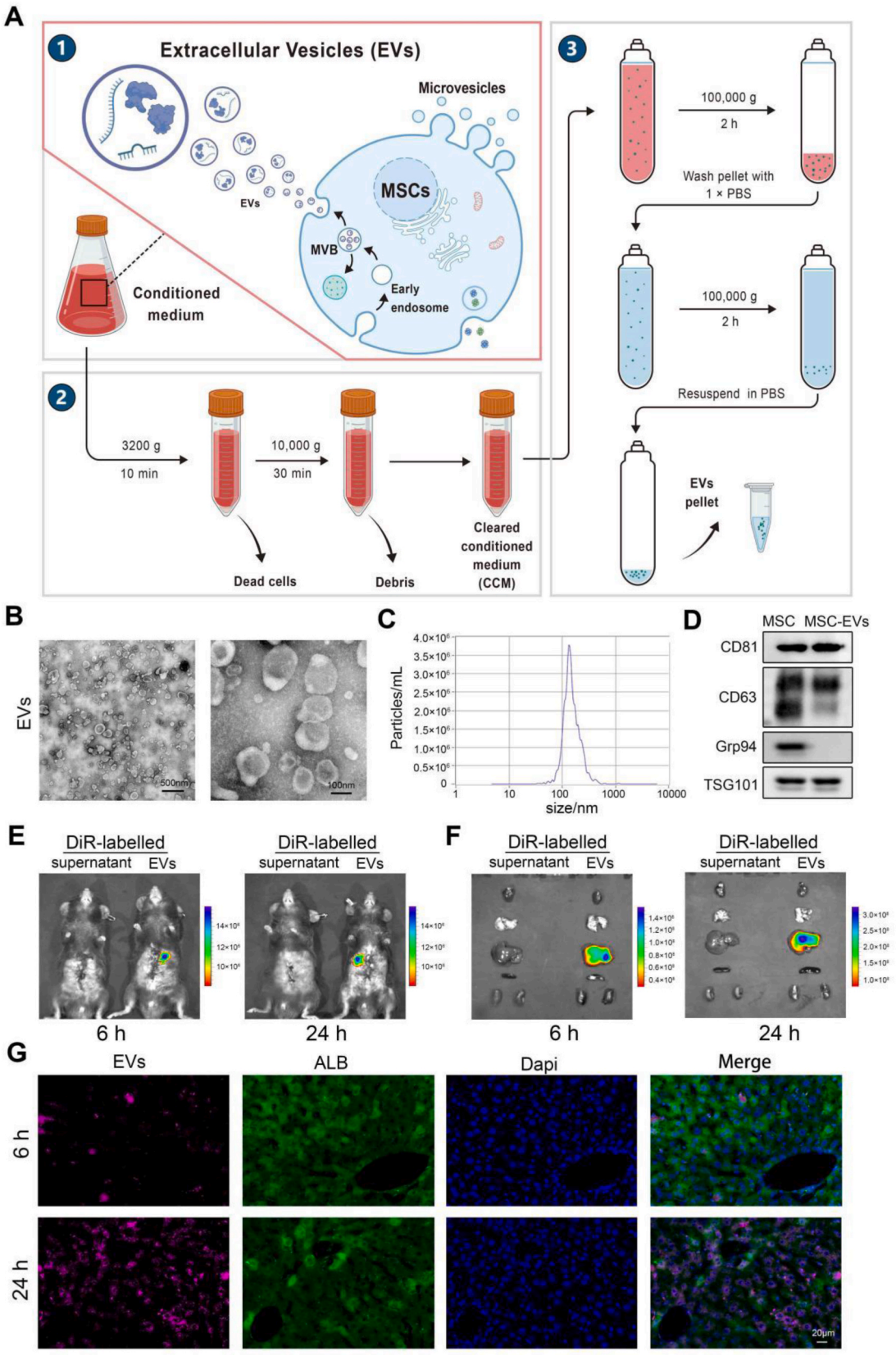

Fig. 1. Extraction procedures and characteristics of MSC-EVs and their distribution in the aged HIRI. **A**: The purification process of MSC-EVs. **B**: Representative images of TEM to show the morphology of MSC-EVs (Left, scale bar = 500 nm. Right, scale bar = 100 nm). **C**: NTA assays showing the size distribution of MSC-EVs. **D**: Western blotting assays showing the characterization of MSCs and MSC-EVs. **E-F:** DiR-labeled MSC-EVs accumulated in the liver of aged HIRI model, shown by *in vivo* (E) and *in vitro* (F) fluorescence at 6 and 24 h (n = 3, per group). **G**: Representative images of IF staining assays showing the distribution of DiR-EVs in hepatocytes (scale bar = 20 μm). All *in vitro* experiments were repeated at least three times.

from the Model Animal Research Center of Nanjing University (Nanjing, China). Animals were housed in the Experimental Animal Center of Sun Yat-sen University under specific pathogen-free (SPF) conditions (22 °C, 50 % humidity, 12-h light/dark cycle) and provided with standard rodent chow and water *ad libitum*. All procedures were performed in accordance with the Guidelines for Animal Experimentation of Sun Yat-sen University and approved by the Animal Care and Use Committee of Third Affiliated Hospital of Sun Yat-sen University (Guangzhou, China), adhering to relevant Chinese legislation regarding the use of experimental animals.

2.5. Establishment of the mouse HIRI model

The establishment of the mouse HIRI model followed a previously described protocol [13]. Briefly, mice were anesthetized with sodium pentobarbital (100 μL/10 g body weight, 1 % solution) and subjected to a laparotomy. Atraumatic vascular clamps were then applied to the vessels supplying the middle and left hepatic lobes for 90 min to induce ischemia. Reperfusion was initiated by clamp removal. At pre-determined time points, mice were euthanized, and serum and liver tissue samples were collected.

2.6. Tracking MSC-EVs in the aged HIRI model

To investigate the distribution of MSC-EVs in the aged HIRI model, MSC-EVs were labeled with the lipophilic dye 1,1′-dioctadecyl-3,3,3′,3′-tetramethylindotricarbocyanine iodide (DiR; Thermo Fisher Scientific, USA) according to the manufacturer's protocol. The resulting DiR-labeled MSC-EVs were then administered to the aged HIRI model via tail vein injection. *In vivo* biodistribution of MSC-EVs at selected time points was assessed using a Bruker Small Animal Optical Imaging System (In-Vivo Xtreme II; Billerica, MA). Subsequently, the heart, lung, liver, spleen, and kidneys were harvested from each mouse, and the fluorescence intensity of DiR-labeled MSC-EVs in these organs was measured using the same imaging system.

2.7. Assessment of liver injury

Serum ALT, AST, and lactate dehydrogenase (LDH) activities were measured using an A7180 Biochemical Analyzer (Hitachi, Japan). Liver samples were fixed in 4 % paraformaldehyde (PFA), embedded in paraffin, sectioned at 4 μm thickness, and stained with hematoxylin and eosin (H&E). Two independent investigators, blinded to the experimental groups, assessed the severity of hepatic injury in each sample using a light microscope (Leica, Germany). Hepatic injury was histologically scored according to Suzuki's criteria. For each section, five randomly selected fields were evaluated and assigned a score of 0, 1, 2, 3, or 4. The final Suzuki score for each section was determined by calculating the mean score of the five fields.

2.8. Immunohistochemistry (IHC) staining

Four-micrometer liver sections were deparaffinized, rehydrated, subjected to antigen retrieval using sodium citrate buffer, and blocked with QuickBlock Blocking Buffer (Beyotime, Shanghai, China). Subsequently, sections were incubated overnight at 4 °C with a primary antibody against SLC39A14 (1:50; Affinity, Australia), followed by a 1-h incubation with a secondary antibody and staining with a Dako REAL EnVision Detection System (Copenhagen, Denmark). IHC scoring was performed by two pathologists blinded to the experimental groups, evaluating five fields per section. The IHC score was calculated as the product of IHC staining intensity and staining area. IHC staining intensity was graded as strong (4), moderate (3), weak (2), or negative (1). The staining area was scored based on the percentage of positively stained cells: 75–100 % (4), 50–75 % (3), 25–50 % (2), and 0–25 % (1).

2.9. Western blotting assay

Samples were lysed with cold radioimmunoprecipitation assay (RIPA) buffer containing a protease inhibitor cocktail (KeyGEN BioTECH, Jiangsu, China), 10 % sodium dodecyl sulfate (SDS), 0.1 % Triton X-100, 2 mM ethylenediaminetetraacetic acid (EDTA), 50 mM Tris-HCl (pH 7.4), 10 % sodium deoxycholate, and 150 mM NaCl. The resulting lysates were then subjected to 10 % SDS-polyacrylamide gel electrophoresis (PAGE) to separate proteins, followed by transfer to polyvinylidene difluoride (PVDF) membranes (Millipore, Billerica, MA, USA). Membranes were blocked with 5 % nonfat milk for 1 h at room temperature and incubated overnight at 4 °C with primary antibodies against: ACSL4 (1:1000; Abcam, Cambridge, UK); CDGSH iron-sulfur domain-containing protein 1 (CISD1; 1:1000; Abcam, Cambridge, UK); ferritin heavy chain 1 (FTH1; 1:1000; Abcam, Cambridge, UK); GPX4; 1:1000; Abcam, Cambridge, UK); nuclear factor erythroid 2-related factor 2 (NRF2; 1:1000; Affinity, Australia); solute carrier family 39 member 4 (SLC39A14; 1:1000; Affinity, Australia); CD81 (1:1000; Abcam, Cambridge, UK); CD63 (1:1000; Abcam, Cambridge, UK); glucose-regulated protein 94 (GRP94; 1:1000; Abcam, Cambridge, UK); and tumor susceptibility gene 101 protein (TSG101; 1:1000; Abcam, Cambridge, UK). After washing, membranes were incubated with horseradish peroxidase (HRP)-conjugated secondary antibodies (anti-mouse IgG [1:5000; Cell Signaling Technology] or anti-rabbit IgG [1:5000; Sigma-Aldrich]) for 1 h at room temperature with gentle agitation. Immunoreactive bands were visualized using an enhanced chemiluminescence substrate (ECL; Merck KGaA, Darmstadt, Germany) and a ChemiDoc™ MP Imaging System (Bio-Rad, CA, USA).

2.10. Total RNA extraction and quantitative real-time polymerase chain reaction (RT-qPCR)

Total RNA was extracted using TRIzol® Reagent (Invitrogen, Life Technologies, USA) according to the manufacturer's protocol. RNA purity and concentration were determined using a UV–visible spectrophotometer (BioMate 3S, Thermo Scientific, USA). RNA was reverse-transcribed to cDNA using a Transcriptor First Strand cDNA Synthesis Kit (Roche Applied Science, USA). Subsequently, cDNA templates were amplified using a PCR Thermal Cycler (Bio-Rad, USA). Quantitative real-time PCR was performed using a SYBR® Green Master Mix (Roche Applied Science) and a LightCycler® 480 System (Roche, USA). β-actin served as an internal control. All primers used in this study were designed and purchased from RiboBio Co., Ltd. (Guangzhou, China). The primer sequences are listed in Table S1 of Supplementary file.

2.11. Quantification of oxidative stress markers

Malondialdehyde (MDA), superoxide dismutase (SOD), and glutathione (GSH) concentrations in each group were determined in liver tissue homogenates. Briefly, liver tissues were homogenized in cold saline (10 % *w/v*), and the resulting supernatants were assayed for MDA, SOD, and GSH using commercially available kits (Jiangcheng Bioengineering Institute, Nanjing, China) according to the manufacturer's instructions.

Dihydroethidium (DHE; MCE, NJ, USA) was used to measure reactive oxygen species (ROS) generation. Samples were incubated with pre-warmed DHE for 30 min at 37 °C in the dark and then imaged using a fluorescence microscope with excitation/emission wavelengths of 518/616 nm. Five fields of view were imaged per sample, and the mean DHE fluorescence intensity was calculated by averaging the values from these five fields. Intracellular ROS detection was performed using a 585/42 nm bandpass filter for DHE fluorescence. Data were expressed as mean fluorescence intensity (MFI).

2.12. Lipid peroxidation analysis

To assess the degree of lipid peroxidation, samples were incubated with C11-BODIPY reagent (GLPBIO, Montclair, CA) for 30 min at 37 °C in the dark, gently washed with phosphate-buffered saline (PBS), fixed with 4 % PFA, and mounted with a 4′,6-diamidino-2-phenylindole (DAPI)-containing mounting medium. Samples were then examined using an upright epifluorescence microscope (Leica, Germany). A shift in fluorescence from magenta to green indicated a transition from non-oxidized to oxidized lipids. In tissue samples, the ratio of oxidized lipids was determined by dividing the number of cells exhibiting lipid peroxidation by the total number of cells. Five fields were imaged per sample, and the final ratio of oxidized lipids for each sample was calculated as the average of the ratios from the five fields. In primary cells and organoids, lipid peroxidation was quantified by calculating the ratio of mean green fluorescence intensity (oxidized BODIPY C11 [excitation/emission: 581/591 nm]) to mean red fluorescence intensity (reduced BODIPY C11 [excitation/emission: 581/591 nm]) per cell.

2.13. RNA sequencing and bioinformation analysis

Total RNA was extracted from liver tissues, and mRNA was purified using poly(T) oligo-attached magnetic beads. cDNA libraries were constructed using the NEBNext® Ultra™ RNA Library Prep Kit for Illumina® (New England Biolabs [NEB], Ipswich, MA, USA). Sample clustering was performed using a cBot Cluster Generation System with the TruSeq PE Cluster Kit v3-cBot-HS (Illumina, San Diego, CA, USA). Libraries were sequenced on an Illumina NovaSeq platform, generating 150 bp paired-end reads. For data analysis, quality control was initially performed to obtain clean reads by removing low-quality reads from the raw data. Clean reads were then aligned to the reference genome obtained from an appropriate genome database. Gene-level read counts were quantified using featureCounts (v1.5.0-p3). Differential gene expression analysis was performed using the DESeq2 R package (version 1.16.1) was used to compare. The *p*-values were adjusted for multiple testing using the Benjamini-Hochberg method to control the false discovery rate (FDR). Kyoto Encyclopedia of Genes and Genomes (KEGG) and Gene Ontology (GO) pathway enrichment analyses were performed using the clusterProfiler R package.

2.14. Animal adeno-associated virus-8 (AAV8) injection and processing

AAV8 generation: siRNA targets were designed based on SLC39A14 transcripts and primers were arranged for synthesis. The single-stranded primers were annealed into double-stranded Oligo sequences and connected to the double-enzymatic linear zed RNA interference vector (Hanbio Biotechnology Co., Ltd.). Knockdown efficiency was evaluated by by measuring the reduction in Enhanced Green Fluorescent Protein (EGFP) fluorescence of HEK293 cells, which were co-transfected with an EGFP-tagged SLC39A14 expression vector and individual SLC39A14-shRNA expression vectors. The most effective sequence was chosen and the selected oligos were then cloned into the linear zed pHBAAV-U6-MCS-CMV-EGFP vector (Hanbio Biotechnology Co., Ltd.) using T4 DNA ligase.

AAV8-SLC39A14 (1×10^{12} viral genomes·mL^{-1}, sequence: NM_144808.4:259–1728 (detailed sequence included in Table S2 of supplementary file)) and AAV8-shSLC39A14 (1×10^{12} viral genomes·mL^{-1}, sequence: 5′-GCAGGCTCTCTTCTTCAACTT-3′), purchased from Hambio Biotechnology (Vectors: pHBAAV-U6-MCS-CMV-EGFP, pAAV-RC, pHelper, Shanghai, China), were administrated through the tail intravenous injection to specially overexpress or downregulate the expression of hepatocellular SLC39A14 *in vivo*. The mice were injected with AAV8-empty vectors as normal control groups. As AAV8 contains the green fluorescent protein gene (GFP), biodistribution was assessed four weeks post-injection using a Bruker small animal optical imaging system. The efficacy of SLC39A14 overexpression and knockdown was confirmed by RT-qPCR and Western blot analysis.

2.15. Isolation and identification of mouse primary hepatocytes

Primary hepatocytes were isolated from 20- to 24-month-old C57BL/6 mice. Following perfusion via the portal vein with pre-warmed Hanks' Balanced Salt Solution (HBSS; Thermo Fisher Scientific, UK) containing collagenase type H (1 mg/mL; Sigma-Aldrich, St. Louis, MO, USA), livers were excised and dissociated through a 70-μm cell strainer. Samples were centrifuged at 50×*g* for 5 min at 4 °C, the supernatant was discarded, and the cell pellet was resuspended in complete medium. This suspension was gently overlaid onto 90 % Percoll (GE Healthcare, USA) and centrifuged at 200×*g* for 10 min at 4 °C to isolate primary hepatocytes. The resulting cell pellet was cultured in DMEM/Ham's F-12 medium (Thermo Fisher Scientific, UK) supplemented with 10 % fetal bovine serum (Gibco, Carlsbad, CA, USA), 1 % penicillin-streptomycin, 100X Insulin-Transferrin-Selenium (Gibco, Carlsbad, CA, USA), and 100 nM dexamethasone (Sigma-Aldrich) in a humidified incubator at 37 °C with 5 % CO_2. Immunofluorescence (IF) staining for cytokeratin 18 (CK18) was performed to assess the purity of the isolated primary hepatocytes.

2.16. The construction and culture of human liver organoids (hLOs)

Next, hLOs were generated from liver tissue obtained during hepatectomy procedures from three independent older patients (≥60 years of age) at the Department of Liver Surgery, Third Affiliated Hospital of Sun Yat-sen University (Guangzhou, China). The Ethics Committee of Third Affiliated Hospital of Sun Yat-sen University (Guangzhou, China) approved the use of these samples for research, and all patients provided informed consent. The University of Wisconsin solution (also named UW solution) refers to the preservation solution used to preserve the donor organ during organ transplantation [28,29]. In this study, the liver tissues obtained from the operating room was promptly preserved in the UW solution at 4 °C for transportation to the laboratory. Subsequently, the tissue was enzymatically digested with collagenase/Accutase, washed with DMEM/F-12 at 4 °C, and centrifuged at 400×*g* for 5 min. The resulting cell pellets were resuspended in Matrigel (Corning, New York, USA) and seeded in 48-well plates at a density of 10,000 cells/-well. After 14 days, the organoids were mechanically dissociated into smaller fragments, washed in DMEM/F-12 at 4 °C, resuspended in Matrigel, and cultured in a human liver organoid medium (ORGEN BIOTECH, Guangzhou, China).

2.17. β-galactosidase (β-gal) assay

β-galactosidase activity in primary hepatocytes was assessed using a Senescence Cells Histochemical Staining Kit (Sigma-Aldrich, St. Louis, MO, USA) according to the manufacturer's instructions. Following two washes with PBS, samples were fixed with fixation buffer for 5 min at room temperature. Subsequently, samples were incubated with staining mixture (pH 6.0) overnight at 37 °C. Microscopic analysis was performed using an inverted light microscope (Leica, Germany).

2.18. Establishment of hypoxia-reoxygenation (H/R) model

The H/R model, designed to replicate HIRI as previously described [12], was implemented as follows. Samples were initially cultured in a serum-free medium and subjected to a hypoxic environment (1 % O_2, 5 % CO_2, 94 % N_2) for a period of 4 h. Subsequently, the medium was replaced with a complete medium, and samples were transferred to a normoxic incubator for a 2-h reoxygenation period.

2.19. TEM assays

Fresh tissue blocks, not exceeding 1 mm^3 in size, were rapidly excised using a sharp blade within a timeframe of 1–3 min. Subsequently, these blocks were post-fixed in 1 % osmium tetroxide (OsO_4) in 0.1 M phosphate buffer (PB, pH 7.4) for 2 h at room temperature, protected from light. Further sample processing was performed by Servicebio (Wuhan, China). Transmission electron microscopy was employed to examine mitochondrial ultrastructural alterations and evaluate the extent of ferroptosis in the designated samples.

2.20. Calcein-AM/PI double staining

To quantify the extent of *in vitro* cell death, a Calcein-AM/propidium iodide (PI) staining assay was performed. Following treatment according to the experimental design, samples were washed with PBS, incubated with calcein AM and PI (1:1,000, Beyotime, China) at 37 °C for 30 min, and subsequently analyzed using an Incucyte® Live-Cell Analysis system (Sartorius, Germany) to distinguish live (green fluorescence) and dead (red fluorescence) cells. The cell death ratio was calculated as the number of dead cells divided by the total cell count. Five fields of view were imaged per sample, and the final reported cell death ratio for each sample represents the average of these five measurements.

2.21. If staining

Following fixation in 4 % PFA for 30 min and permeabilization with 0.5 % Triton X-100 for 5 min at ambient temperature, samples underwent a blocking step with 3 % bovine serum albumin (BSA) to mitigate non-specific antigen binding. Subsequently, samples were incubated with primary antibodies at 4 °C overnight (Alb; 1:200; Abcam, Cambridge, UK; CK18; 1:200; Abcam, Cambridge, UK; HNF4-α; 1:200; Abcam, Cambridge, UK; Ki67; 1:200, Abcam, Cambridge, UK; LGR5, 1:100; Abcam, Cambridge, UK), followed by incubation with fluorescently labeled secondary antibodies (1:500, Invitrogen, USA) for 1 h at room temperature under dark conditions. Nuclear counterstaining was performed using DAPI for 2 min at room temperature. Imaging was conducted using a confocal microscope (Zeiss 880, Nikon Instruments, Melville, New York, USA).

2.22. Microarray analysis of miRNAs

Total RNA was extracted from MSC-EVs using TRIzol reagent. RNA quantity and quality were subsequently determined using a NanoDrop ND-1000 spectrophotometer, while RNA integrity was assessed via denaturing agarose gel electrophoresis. Samples were then labeled with Cyanine 3-pCp using T4 RNA ligase. Following concentration, drying, and resuspension, the labeled complementary RNA (cRNA) was fragmented using a Blocking Agent and Fragmentation Buffer, incubated at 60 °C for 30 min, and diluted in GE hybridization buffer. This hybridization solution was applied to gene expression microarray slides and incubated for 17 h at 65 °C in an Agilent Hybridization Oven. Post-hybridization, arrays were washed, stabilized, and scanned using the Agilent Microarray Scanner. Array image analysis was performed using Agilent Feature Extraction software (version 11.0.1.1). Quantile normalization and data processing were conducted using the GeneSpring GX v12.1 software package (Agilent Technology). Detected microRNAs (miRNAs) were selected for subsequent analysis.

2.23. Dual-luciferase reporter assay

To investigate the interaction between miR-1275 and its target gene, *SLC39A14*, two plasmids were generated: a wild-type construct (SLC39A14-3′UTR-WT) and a mutant construct harboring alterations within the miR-1275 binding site of the SLC39A14 3′UTR (SLC39A14-3′UTR-MUT). These constructs were subsequently cloned into a luciferase reporter vector (GeneChem, Shanghai, China). HEK-293T cells were co-transfected with either the wild-type or mutant SLC39A14 plasmids and either a negative control (NC) or miR-1275 mimic or miR-1275 inhibitor, using Lipofectamine 3000 (Invitrogen, USA). Luciferase activity was then assessed using a dual-luciferase reporter assay system (Promega, USA), with Renilla luciferase serving as an internal control. Luminescence measurements for both Firefly and Renilla luciferase were conducted according to the manufacturer's protocol.

2.24. RNA fluorescence in situ hybridization (RNA-FISH)

RNA-FISH was carried out to investigate the distribution of miR-1275 in MSCs using a Fluorescent in Situ Hybridization Kit (RiboBio, Guangzhou, China) according to the previously described [30]. After that, the cells were observed under a Zeiss 880 confocal microscope (Nikon Instruments, Melville, New York, USA).

2.25. miRNA treatment

Mimic or inhibitor molecules of miR-1275, procured from RioBio (Guangzhou, China), were introduced into specified cell lines to induce overexpression or knockdown of miR-1275, respectively. Transfection was performed using Lipofectamine 3000 (Invitrogen, USA) according to the manufacturer's instructions. Cells were transfected at 80–90 % confluence. Following a 48-h transfection period, the culture medium was replaced with DMEM supplemented with 10 % FBS for subsequent experimentation.

2.26. Assessment of iron concentration levels

1) Iron levels in liver tissue were assessed via Perl's Prussian blue staining. Tissue sections mounted on slides were processed as follows: Following staining, slides were rinsed with distilled water and incubated in a 0.3 % hydrogen peroxide (H_2O_2) solution in methanol for 20 min to quench endogenous peroxidase activity. Subsequently, an intensifying solution (PBS containing 0.05 % 3,3′-Diaminobenzidine [DAB], 0.025 % cobalt chloride [$CoCl_2$], and 0.015 % H_2O_2) was applied for 15 min, and the reaction was terminated by rinsing with distilled water. Finally, slides were counterstained with either hematoxylin QS or neutral red and examined using an inverted microscope.
2) The Iron Assay Kit (Abcam, USA) was also employed to determine the iron concentration in a series of *in vivo* and *in vitro* experiments according to the manufacturer's instructions. The assay was performed as follows: standard wells were prepared by aliquoting 100 μL of serially diluted iron standard solutions, while sample wells were loaded with 2–50 μL of experimental samples, with volumes adjusted to 100 μL/well using Iron Assay Buffer. Subsequently, 5 μL of Iron Reducer was added to all standard wells, and for iron (II)-specific quantification, 5 μL of Assay Buffer was added to sample wells. The plate was thoroughly mixed and incubated at 37 °C for 30 min under standard atmospheric conditions. After incubation, 100 μL of Iron Probe was added to each well, and the plate was protected from light, gently mixed, and further incubated at 37 °C for 60 min. Absorbance was immediately quantified using a microplate reader at an optical density of 593 nm (OD593). The iron quantification data were analyzed according to absorbance values.

2.27. RNA knockdown and overexpression

Plasmids for human SLC39A14 knockdown (sh-SLC39A14) and overexpression (oe-SLC39A14) were designed and produced by Miaoling Biology (Wuhan, China). The plasmid sequences are as follows: sh-SLC39A14: pLV3-U6-SLC39A14(human)-shRNA-CopGFP-Puro. oe-SLC39A14: pLV3-CMV-SLC39A14(human)-3 × FLAG-CopGFP-Puro.

Plasmid transfection was carried out using ViaFect Transfection Reagent (Promega, Madison, WI, USA) following the manufacturer's protocol. For siRNA-mediated knockdown, Lipofectamine 3000 reagent (Invitrogen, Carlsbad, CA, USA) was utilized according to the standard procedures. Following a 48-h transfection period with either plasmids or siRNAs (concentration: 50 nmol/L), the cells were subsequently exposed to hypoxia/reoxygenation (H/R). The efficiency of overexpression and knockdown was confirmed through Western blot analysis and quantitative reverse transcription polymerase chain reaction (qRT-PCR).

2.28. RNA immunoprecipitation

RNA immunoprecipitation was performed as described previously [31]. Cells were co-transfected with HA-Ago2 and 100 nM miR-1275 mimic or inhibitor. Subsequently, cells were lysed in a buffer containing 10 mM HEPES (pH 7.4), 0.5 % NP-40, 100 mM KCl, and 5 mM $MgCl_2$. HA-Ago2 immunoprecipitation was performed using an HA-antibody. Protein A agarose was used to capture the immune complex, followed by six washes with a buffer containing 5 mM MgCl2, 10 mM HEPES (pH 7.4), 150 mM KCl, and 0.1 % NP-40. Co-immunoprecipitated RNAs were eluted using TRIzol reagent (Thermo Fisher, USA). The relative enrichment of SLC39A14 and miR-1275 in the RNA-induced silencing complex (RISC) was determined by RT-qPCR. GAPDH was used as a negative control.

2.29. Statistical analysis

The data are expressed as mean ± standard deviation (SD) or individual values, as appropriate. Statistical comparisons between two groups were performed using unpaired two-tailed Student's t-tests, whereas comparisons involving multiple groups were analyzed by one-way analysis of variance (ANOVA). All statistical analyses were performed using GraphPad Prism 8 software (San Diego, CA). The number of biological replicates is indicated in the figure legends. A p-value <0.05 was considered statistically significant.

3. Results

3.1. Characterization of MSC-EVs and their distribution in the aged HIRI

In the present study, MSCs isolated from umbilical cords exhibited a fibroblast-like morphology and demonstrated the capacity to differentiate into adipogenic and osteogenic lineages (Supplementary Figs. 1A–1B). Flow cytometry analysis confirmed the MSC phenotype, characterized by positive expression of CD73, CD90, and CD105, while simultaneously demonstrating negative expression of CD11b, CD19, CD45, CD34, and HLA-DR (Supplementary Fig. 1C). Subsequently, MSC-conditioned medium (MSCs-CM) was collected and subjected to a series of ultracentrifugation steps to isolate MSC-EVs (Fig. 1A). Transmission electron microscopy (TEM) revealed that the MSC-EVs had a round morphology with a distinct bilayer membrane (Fig. 1B). The size distribution of the MSC-EVs ranged from 30 to 150 nm (Fig. 1C). Western blot analysis further corroborated the isolation of MSC-EVs, demonstrating the presence of exosomal markers, including CD81, CD63, and TSG101, while simultaneously confirming the absence of the endosomal marker Grp94 (Fig. 1D). Collectively, these findings demonstrated the successful isolation of MSC-EVs.

To visualize the distribution of MSC-EVs in the aged HIRI model, we labeled them with DiR dye and subsequently administered them to the HIRI model via tail vein injection. At 6 and 24 h post-administration of DiR-labeled MSC-EVs, *in vivo* fluorescence imaging revealed a strong fluorescent signal concentrated in the liver at both time points (Fig. 1E). These findings were corroborated by *in vitro* fluorescence imaging of heart, lung, liver, spleen, and kidney tissues (Fig. 1F). Furthermore, fluorescence staining of tissue sections demonstrated that the punctate DiR fluorescent hotspots were predominantly localized within hepatocytes (ALB-positive cells) (Fig. 1G).

3.2. MSC-EVs attenuate aged HIRI by inhibiting ferroptosis

To investigate the effects of MSC-EVs on the attenuation of aged HIRI, we treated an aged HIRI model with MSC-EVs. Serum and liver tissues were collected at 12 h after treatment (Fig. 2A). As depicted in Fig. 2B–D, serum levels of ALT, AST, and LDH were significantly elevated in the aged HIRI group compared to the normal group. MSC-EVs treatment significantly attenuated this elevation. H&E staining revealed significant pathological changes associated with aged HIRI, including necrotic areas, disrupted hepatic lobules, and inflammatory cell infiltration. These pathological alterations were significantly ameliorated by MSC-EVs treatment, as evidenced by a reduced Suzuki score (Fig. 2E–F).

Next, C11 BODIPY staining was used to assess lipid peroxidation, which is a hallmark of ferroptosis. The results demonstrated increased lipid peroxidation in the aged HIRI group compared to the normal group, which was significantly suppressed by MSC-EV treatment (Fig. 2G–H). Furthermore, Western blot analysis revealed that aged HIRI was associated with downregulated expression of ferroptosis-inhibitory proteins (NRF2, FTH1, GPX4) and upregulated expression of ferroptosis-promoting molecules (CISD1, TFRC, ACSL4). MSC-EV treatment effectively reversed these alterations (Fig. 2K and Supplementary Fig. 2E). Dihydroethidium (DHE) staining and biochemical assays for MDA, GSH, and SOD were performed to evaluate oxidative stress. The results demonstrated a significant increase in ROS production in the liver tissues of the aged HIRI group. MSC-EV treatment effectively suppressed ROS production of aged HIRI (Fig. 2I–J and 2L-2N).

To further investigate whether the protective effects of MSC-EVs in HIRI of aged HIRI are mediated by ferroptosis inhibition, we co-administered MSC-EVs with erastin, a known ferroptosis inducer by downregulating SLC7A11, to treat aged HIRI. SLC7A11 (also known as xCT), as the functional subunit of system xc−, is demonstrated to facilitate cystine uptake for glutathione (GSH) synthesis. Previous studies have demonstrated that Erastin-mediated SLC7A11 inhibition could drive ferroptosis (the upregulation of TFRC, ACSL4, and CISD1 and the degradation of GPX4, NRF2, and FTH1) through the depletion of glutathione, lipid metabolism reprogram, accumulation of lipid peroxides, and the disruption of iron homeostasis [32–38]. We first confirmed that erastin induced ferroptosis in our model by assessing SLC7A11 levels under the indicated treatment conditions (Supplementary Figs. 2A–2D). Subsequently, we observed that erastin significantly attenuated the protective effects of MSC-EVs in aged HIRI. This was evidenced by: (1) reversal of the decrease in lipid peroxidation and ROS accumulation, (2) upregulation of ferroptosis-promoting proteins (CISD1, TFRC, ACSL4), and (3) downregulation of ferroptosis-inhibitory proteins (NRF2, GPX4, FTH1) (Fig. 2G–N and Supplementary Fig. 2E). In addition, erastin significantly mitigated the ability of MSC-EVs to improve serum transaminase levels and alleviate liver injury in aged HIRI (Fig. 2B–F). Collectively, these findings provide strong evidence that MSC-EVs exert their protective effects in aged HIRI, at least in part, through the inhibition of ferroptosis.

3.3. MSC-EVs inhibit ferroptosis of aged hepatocytes during hypoxia/reoxygenation (H/R) treatment

Based on the *in vivo* findings, we further validated the efficacy of MSC-EVs in mitigating aged-related HIRI by investigating their effects on ferroptosis *in vitro*. Primary hepatocytes were isolated from aged mice and their physiological characteristics were assessed (Fig. 3A–B and Supplementary Fig. 3A). MSC-EVs labeled with PKH26 were incubated with the isolated aged hepatocytes for 6 h. Confocal microscopy revealed that the PKH26-labeled MSC-EVs (red fluorescence) were effectively internalized by the aged hepatocytes (Fig. 3C). An *in vitro* H/R model was established to simulate HIRI. Aged hepatocytes were

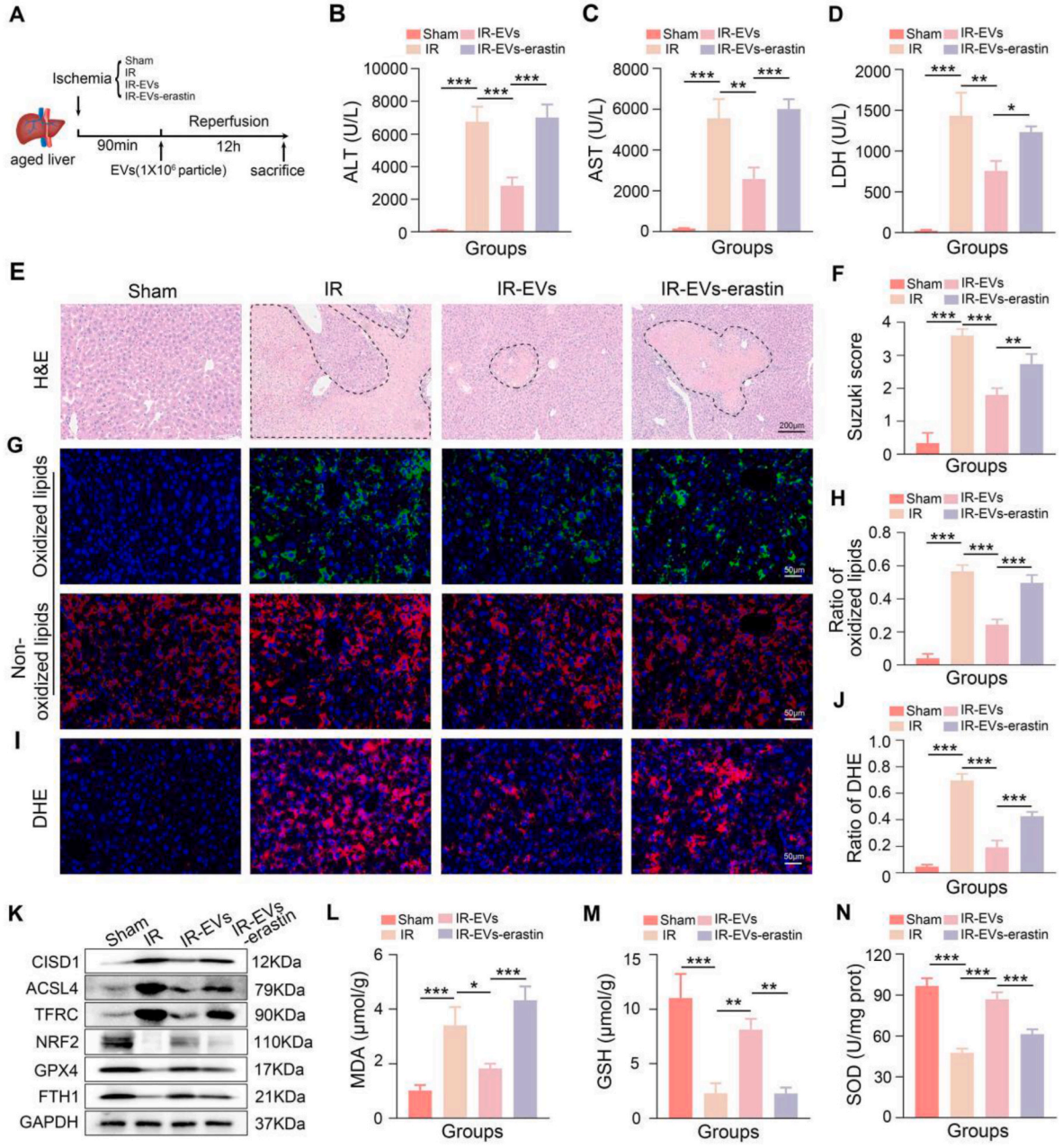

Fig. 2. MSC-EVs alleviates the aged HIRI model by mitigating ferroptosis. **A**: The establishment process of the aged HIRI model. **B-D:** The serum levels of ALT, AST, and LDH of the sham, IR, IR-EVs, and IR-EVs-erastin group (erastin, a ferroptosis activator), (n = 3, per group). **E-J:** The representative images and relative quantification of H&E staining, (scale bar = 200 μm), C11 BODIPY staining (scale bar = 50 μm) and DHE staining (scale bar = 50 μm) in liver tissues with indicated treatments. **K**: The representative western blotting image of the four groups. **L-N:** The levels of MDA, GSH, and SOD in liver tissues with indicated treatments. Statistical significance was determined by one-way ANOVA. Data are expressed as mean ± SD. *p < 0.05, **p < 0.01, ***p < 0.001, and ****p < 0.0001. IR, ischemia reperfusion. EVs, MSC-EVs.

subjected to H/R and subsequently treated with either MSC-EVs or MSC-EVs in combination with erastin. C11 BODIPY and DHE staining demonstrated that H/R induced ferroptosis in aged hepatocytes. MSC-EV treatment effectively attenuated this ferroptosis, while the co-treatment with erastin significantly abrogated the protective effects of MSC-EVs (Fig. 3D–E and Supplementary Figs. 4A–4B). It is well-established that ferroptosis is characterized by morphological changes in mitochondria, including shrinkage and loss of cristae. TEM analysis revealed similar mitochondrial morphological alterations in all four experimental groups (Fig. 3H). Western blot analysis further confirmed the inhibitory effects of MSC-EVs on ferroptosis in the aged H/R model. These effects were significantly attenuated by co-treatment with erastin (Fig. 3I and Supplementary Fig. 4C). In addition, Calcein-AM/PI double staining revealed that the activation of ferroptosis significantly weakened the ability of MSC-EVs to inhibit cell death in aged hepatocytes following H/R injury (Fig. 3F–G).

To further investigate the therapeutic potential of MSC-EVs in an *ex vivo* model, we established aged hLOs using liver tissue samples obtained from patients aged over 60 years who underwent hepatectomy. The detailed procedure for establishing aged hLOs is shown in Supplementary Fig. 5A. As previously reported [39], our aged hLOs exhibited a dense, spheroid-like morphology with a thicker cell layer. Immunofluorescence staining confirmed the expression of hepatocyte-specific markers, such as hepatocyte nuclear factor 4α (HNF-4α) and Albumin

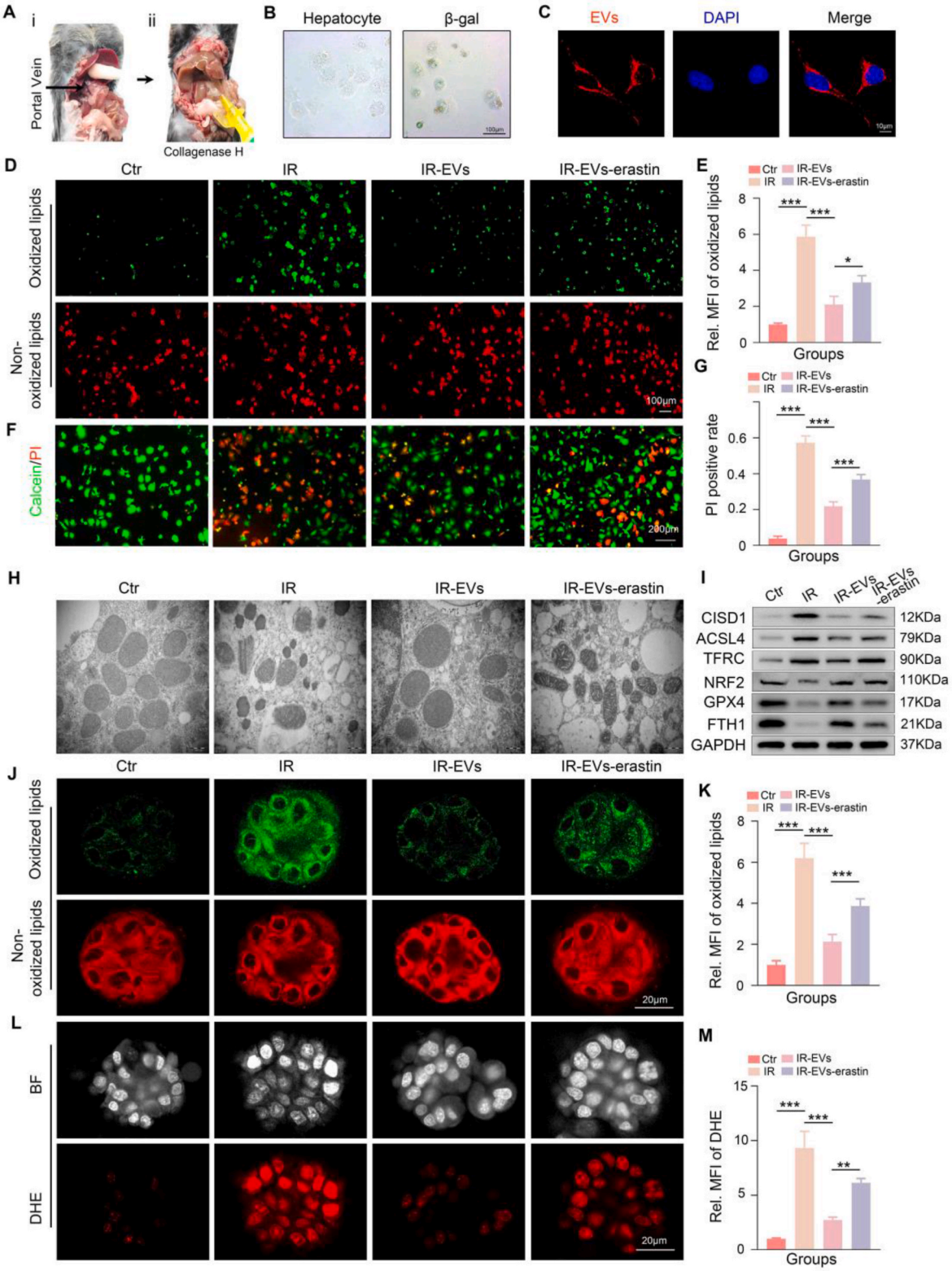

Fig. 3. MSC-EVs inhibit ferroptosis in aged hepatocytes during hypoxia/reoxygenation (H/R) treatment. **A**: Process of isolating primary hepatocytes. **B**: Representative images for the morphology and β-gal staining of aged hepatocytes. **C**: Representative IF images showing the internalization of MSC-EVs labeled PKH26 (red fluorescence) by aged hepatocytes. **D-G**: Representative images and relative quantification of C11 BODIPY staining, and Calcein-AM/PI double staining of the control, IR, IR-EVs, and IR-EVs-erastin groups, scale bar = 200 μm. **H**: Representative TEM assays showing the mitochondrial morphological characteristics in the aged hepatocytes of four groups. **I**: Representative images of western blotting showing the expression of ferroptosis-associated proteins in indicated groups. For aged hLOs H/R model: **J-M**: Representative images and relative quantification of C11 BODIPY staining (scale bar = 20 μm) and DHE staining (scale bar = 20 μm) of the control, IR, IR-EVs, and the IR-EVs-erastin group. Statistical significance was determined by one-way ANOVA. Error bars represent the means of three independent experiments. Data are expressed as mean ± SD. *$p < 0.05$, **$p < 0.01$, ***$p < 0.001$, and ****$p < 0.0001$. MFI, mean fluorescence intensity. Ctr, control. IR, ischemia reperfusion. EVs, MSC-EVs.

(ALB), as well as markers associated with successful organoid formation, including Ki67 and Leucine-rich repeat-containing G-protein coupled receptor 5 (LGR5) (Supplementary Figs. 5B–5C). As shown in Fig. 3J–K, H/R treatment induced ferroptosis in aged hLOs. MSC-EV treatment effectively inhibited ferroptosis, while the addition of erastin significantly reversed this inhibitory effect. Furthermore, MSC-EVs protected aged hLOs from ROS production during H/R, and this protective effect was significantly attenuated by the addition of erastin, as demonstrated by DHE staining (Fig. 3L–M). Collectively, these findings from *in vitro* experiments using both primary hepatocytes and aged hLOs further support the hypothesis that MSC-EVs exert protective effects in aged hepatocytes during H/R injury by inhibiting ferroptosis.

3.4. MSC-EVs suppress iron overload in the aged livers via regulating SLC39A14 expression

To further elucidate the underlying mechanisms by which MSC-EVs inhibit ferroptosis in the aged HIRI model, we performed RNA-sequencing analysis. The unique alteration of 2136 genes were identified in the aged HIRI model, while the expression of 503 genes were modified after treated with MSC-EVs. Of the 2136 genes, 804 were upregulated in the aged HIRI model, whereas 28 were downregulated in the MSC-EV group(Fig. 4A–B). Bioinformatic analysis revealed that the aged HIRI group exhibited significant enrichment in signaling pathways related to “Response to oxidative stress”, “Lipid biosynthetic process”, and “Ferroptosis” compared to the normal group. In contrast, these pathways were not significantly enriched in the MSC-EV-treated group (Fig. 4C). Within the “Ferroptosis” signaling pathway, the expression of SLC39A14 was significantly downregulated in the MSC-EV-treated group compared to the control group. This finding was further validated by IHC and RT-qPCR (Fig. 4D–F). SLC39A14 is a critical iron importer that contributes to intracellular iron overload and subsequent ferroptosis [40]. Consistent with this finding, we observed a significant decrease in iron levels in the aged HIRI model following MSC-EV treatment (Fig. 4G). To further confirm the role of iron accumulation in ferroptosis-mediated aged HIRI, we utilized Deferoxamine (DFO), an iron chelator, as a positive control. As shown in Supplementary Figs. 6A–C, DFO treatment significantly reduced serum levels of ALT, AST, and LDH in the aged HIRI model compared to the IR group. Moreover, histopathological analysis revealed that DFO treatment ameliorated liver injury, with reduced necrotic areas, disrupted hepatic lobules, and inflammatory cell infiltration, along with a reduced Suzuki score (Supplementary Figs. 6F–6G). In addition, C11 BODIPY assays and DHE staining, along with measurements of malondialdehyde (MDA) and superoxide dismutase (SOD) levels, demonstrated that DFO treatment effectively inhibited lipid peroxidation and ROS accumulation in the aged HIRI model (Supplementary Figs. 6D–6E, 6H–6K). Collectively, these findings strongly suggest that iron accumulation plays a pivotal role in ferroptosis-mediated aged HIRI. Furthermore, these results indicate that MSC-EVs may exert their protective effects in aged HIRI by inhibiting SLC39A14-mediated intracellular iron overload.

To further validate the role of SLC39A14 in H/R injury, we transfected aged hepatocytes with shRNA targeting SLC39A14 to knock down its expression (Supplementary Fig. 7A). SLC39A14 sownregulation significantly reduced intracellular iron levels (Fig. 4H) and suppressed ferroptosis in aged hepatocytes following H/R treatment. This was evidenced by decreased C11 BODIPY staining intensity, reduced ROS production (assessed by DHE staining), downregulation of ferroptosis-related proteins, and preservation of mitochondrial morphology with intact cristae (Fig. 4I–J, Supplementary Fig. 8A-8D and 8G). Furthermore, Calcein-AM/PI double staining demonstrated that knockdown of SLC39A14 significantly mitigated cell death in aged hepatocytes during H/R treatment (Supplementary Figs. 8E–8F).

For *in vivo* experiments, we employed hepatotropic AAV to specifically downregulate SLC39A14 expression in hepatocytes. AAV8 was engineered to express GFP, enabling direct visualization of hepatocyte transduction (Supplementary Fig. 9A). RT-qPCR and Western blot analysis confirmed the efficient downregulation of SLC39A14 expression in liver tissues by AAV8-shSLC39A14 (Supplementary Figs. 9B–9E). SLC39A14 knockdown in the aged HIRI model resulted in a significant decrease in iron accumulation and inhibition of ferroptosis (Fig. 4K–P and Supplementary Fig. 9F). Moreover, SLC39A14 knockdown alleviated aged HIRI, as evidenced by reduced serum hepatic enzyme levels and improved hepatic pathology (Supplementary Figs. 10A–10C and Fig. 4Q–R). Furthermore, the inhibitory effects of SLC39A14 silencing on ferroptosis were also observed in the aged hLOs H/R model (Fig. 4S–V).

3.5. SLC39A14 is a critical factor for MSC-EVs to inhibit ferroptosis and alleviate liver injury in the aged HIRI

To further illustrate the role of SLC39A14 in the aged HIRI, we clinically collected pairs of donor liver specimens, from both the pre-perfusion period and reperfusion period, of recipients who received LT in our center and divided them into two group according to the age of the donor (young, age <30 years; old, age ≥ 60 years). Considering the pre-perfusion period as the baseline, we observed a significant increase in SLC39A14 expression and iron overload in liver tissues during the reperfusion period. Notably, these changes were more pronounced in the aged donor group (Fig. 5A–D). Furthermore, recipients with higher SLC39A14 expression in their graft exhibited more obvious elevated serum levels of transaminases on POD1 (Fig. 5E). Additionally, these recipients demonstrated delayed recovery of transaminase levels from POD1 to POD7 (Fig. 5F–G). The above clinical data showed that aged liver was more prone to ferroptosis and high levels of ferroptosis were associated with poor liver function recovery in LT patients. Moreover, we established HIRI models in both young and old animals. Western blot analysis revealed significantly lower levels of GPX4 in the livers of aged animals after reperfusion compared to young animals, accompanied with high levels of ACSL4 and TFRC (Fig. 5H–I). C11 BODIPY staining demonstrated a similar trend, with more obvious increased lipid peroxidation observed in the aged HIRI (Fig. 5J–K).

Subsequently, we overexpressed SLC39A14 in aged hepatocytes to further verify the roles of SLC39A14-related iron overload in MSC-EVs-mediated alleviation of aged HIRI. *In vivo*, we utilized AAV8-SLC39A14. *In vitro*, we transfected cells with plasmids encoding SLC39A14 (Supplementary Fig. 7B and Supplementary Fig. 9A, 9C-9E). As shown in Fig. 6A–B, 6G and Supplementary Figs. 11A–11C and Supplementary Figs. 12A–12B, 12G-12I, overexpression of SLC39A14 significantly abrogated the ability of MSC-EVs to inhibit ferroptosis and reduce iron levels in the aged HIRI model and the aged hepatocyte H/R model. Furthermore, overexpression of SLC39A14 resulted in increased ROS production compared to MSC-EV treatment alone (Fig. 6C–D, 6H–6I and Supplementary Fig. 12C-12D, 12J). Moreover, the hepatoprotective effects of MSC-EVs on aged livers during IR injury were markedly attenuated by the overexpression of SLC39A14 (Fig. 6E–F and Supplementary Figs. 12E–12F, 12K-12 M). Finally, using the aged hLOs H/R model, we further demonstrated that the ability of MSC-EVs to inhibit ferroptosis and mitigate aged HIRI was dependent on its ability to downregulate SLC39A14 expression (Fig. 6J–M).

3.6. MSC-EVs regulate SLC39A14 expression in the aged hepatocytes H/R model via delivery of miR-1275

EVs are recognized as crucial mediators of intercellular communication, as they encapsulate a diverse array of functional components. In previous studies, we demonstrated that MSC-EVs can ameliorate HIRI by delivering beneficial cargoes, including MnSOD, CCT2, and functional mitochondria. Furthermore, we showed that MSC-EVs enhance the proliferative capacity of aged hepatocytes by transferring DDX5 [19–22]. Emerging evidence suggests that MSC-EVs also contain a multitude of miRNAs that exert significant biological functions.

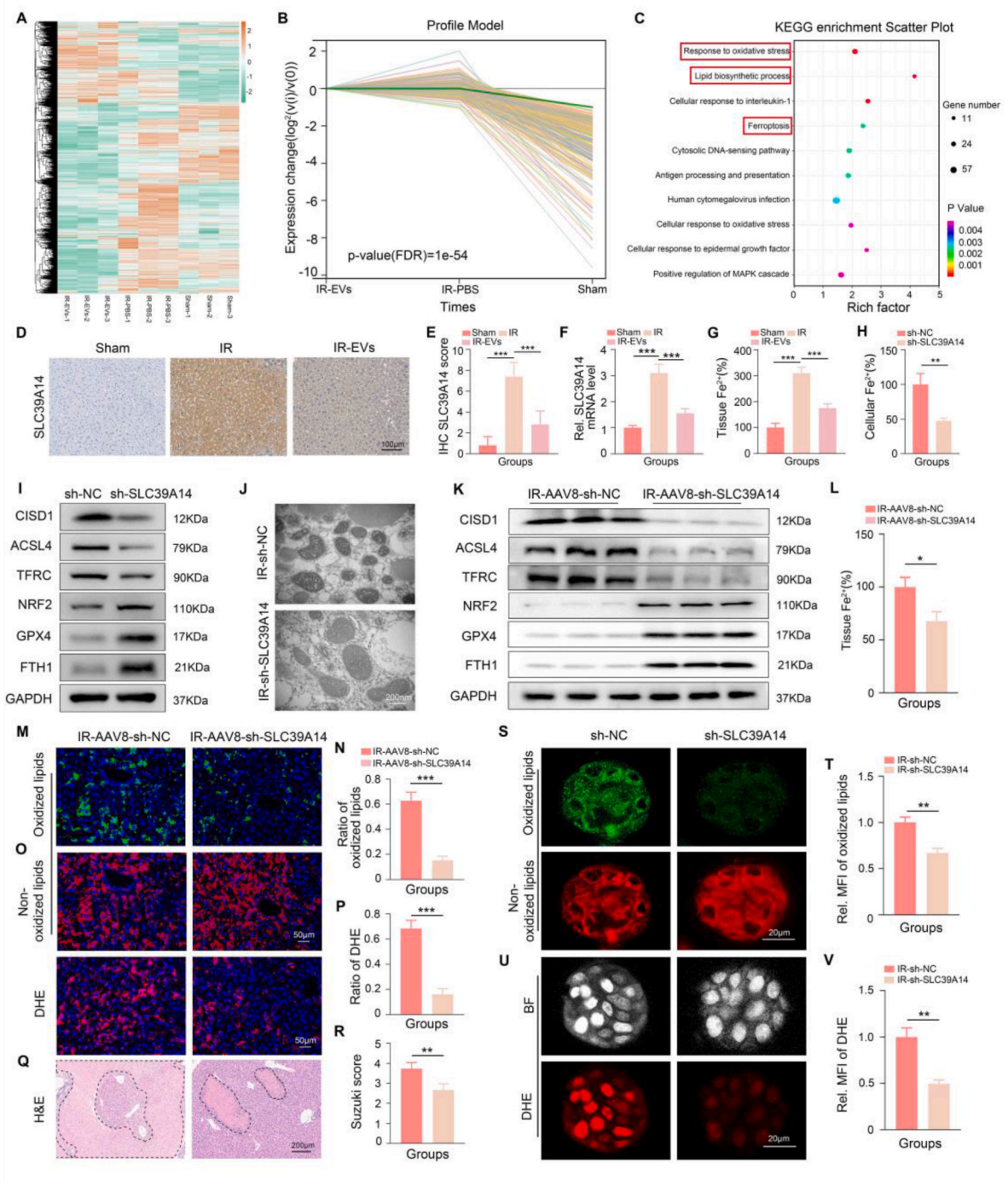

Fig. 4. MSC-EVs suppressed hepatic SLC39A14 expression and iron accumulation in the aged HIRI model. **A-C**: The heat map, the profile model and the KEGG enrichment scatter plot of liver deferentially expressed genes in the Sham, IR and IR-EVs group. **D-E**: The representative images and related quantification of IHC assays showing the SLC39A14 expression in livers with indicated treatments (scale bar = 100 μm). **F**: Relative SLC39A14 mRNA levels in each group. **G**: Tissue iron levels of the Sham, IR and IR-EVs group. **H**: Cellular iron levels in each group. **I**: Western blot analysis depicting the expression levels of ferroptosis-related proteins. **J**: Transmission electron microscopy (TEM) images illustrating the abundance of mitochondria. Scale bar: 200 nm. **K-L:** Representative western blotting images and the tissue iron levels of the IR-AAV8-sh-NC group and the IR-AAV8-sh-SLC39A14 group, (n = 3, per group). **M-R**: Representative images and relative quantification of C11 BODIPY staining, DHE staining, and H&E staining in the two groups (scale bar = 200 μm), (n = 3, per group). **S–V:** Similar results were also evidenced by representative images and relative quantification of C11 BODIPY staining, and DHE staining in aged hLOs with indicated treatments, error bars represent the means of three independent experiments, (scale bar = 20 μm). Statistical significance was determined by one-way ANOVA as appropriate. Data are expressed as mean ± SD. *$p < 0.05$, **$p < 0.01$, ***$p < 0.001$, and ****$p < 0.0001$. MFI, mean fluorescence intensity. IR, ischemia reperfusion. EVs, MSC-EVs. sh-NC, shRNA-normal control. sh-SLC, shRNA-SLC39A14.

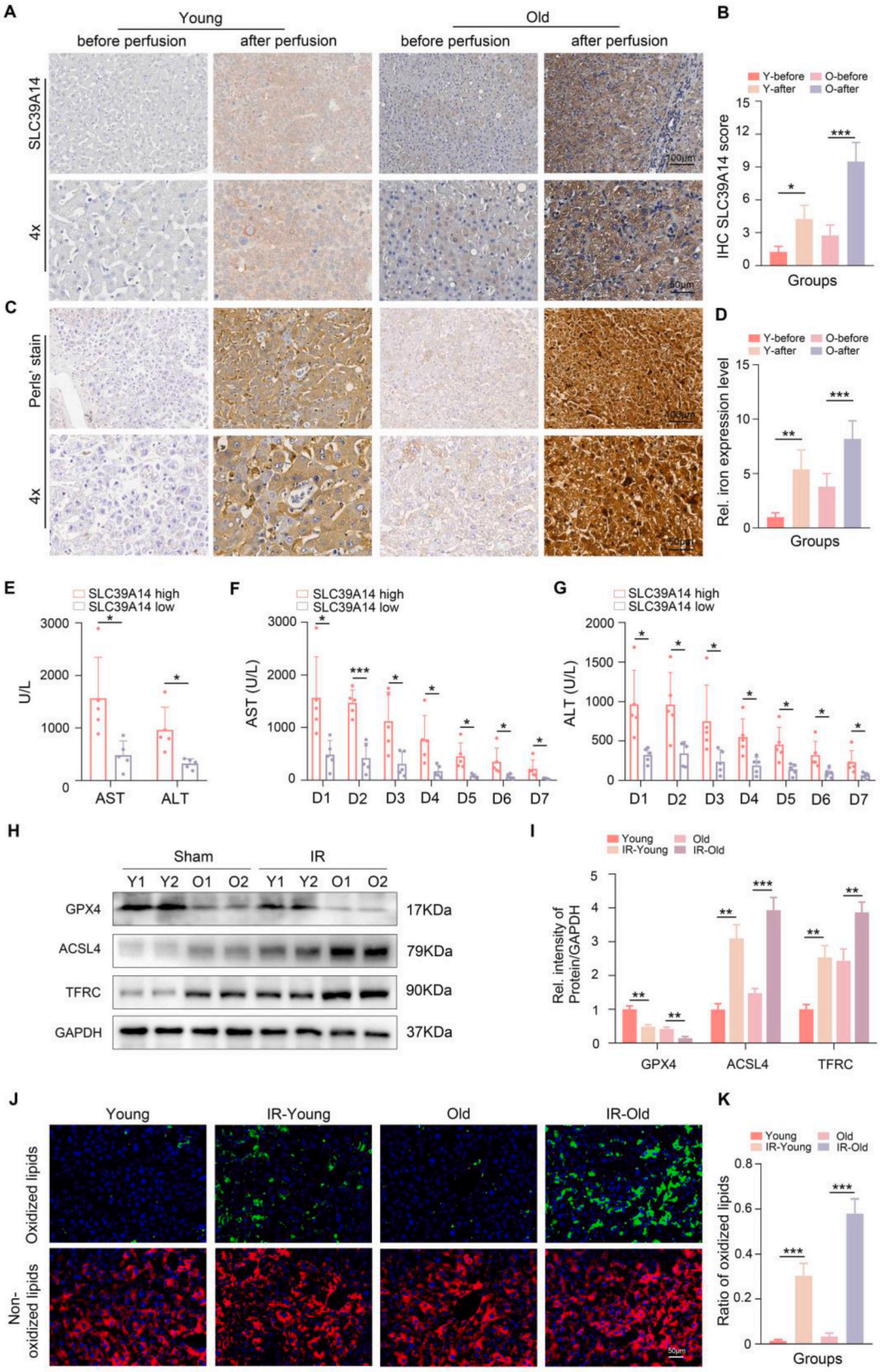

Fig. 5. The clinical significance of SLC39A14 expression in the graft livers following OLT and the ferroptosis levels in young and aged HIRI. **A-D**: Representative images and relative quantification of the SLC39A14 expression and the iron expression level (Perl's stain) in liver tissues before and after reperfusion in young and old group (Up, scale bar = 100 μm, down, scale bar = 50 μm), (n = 3, per group). **E**: Recipients with high SLC39A14 expression showed higher levels of serum ALT and AST at POD1 (n = 5 per group). **F-G:** Recipients with high SLC39A14 expression showed delayed recovery of ALT and AST from POD1 to POD7 (n = 5 per group). **H–K**: Representative images and relative quantification of western blotting assays and C11 BODIPY staining of liver tissues with indicated treatments (n = 3 per group). Data are expressed as mean ± SD. *p < 0.05, **p < 0.01, ***p < 0.001, and ****p < 0.0001. Y, Young. O, Old. IR, ischemia reperfusion.

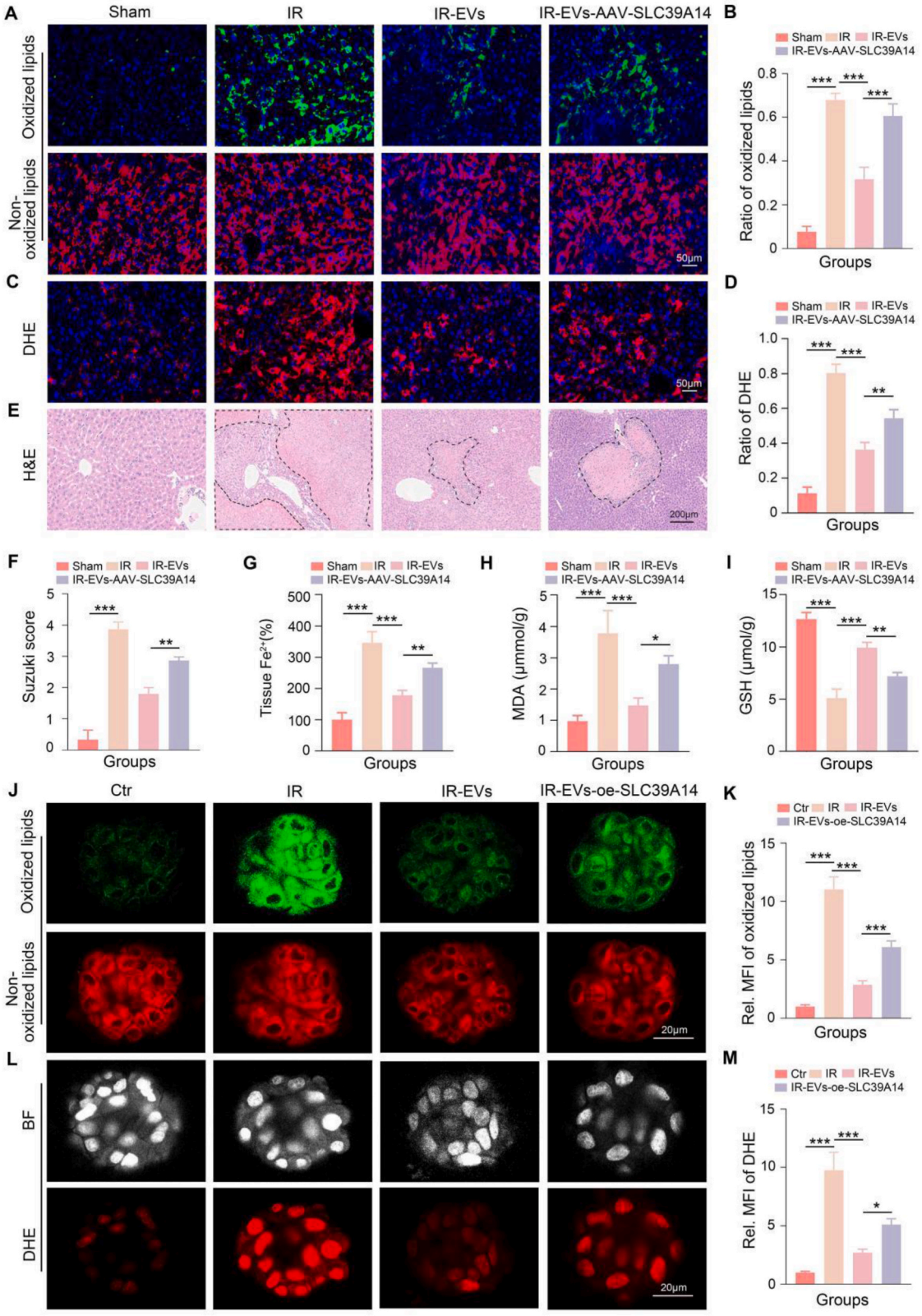

Fig. 6. SLC39A14 is essential for MSC-EVs to attenuate ferroptosis and protect against liver injury in the aged HIRI model. **A-F**: Representative images and relative quantification of C11 BODIPY staining (scale bar = 50 μm), DHE staining (scale bar = 50 μm) and H&E staining (scale bar = 200 μm) of the Sham, IR, IR-EVs, and the IR-EVs-AAV8-SLC39A14 group (n = 3 per group). **G-I**: The levels of Fe^{2+}, MDA and GSH in liver tissues with indicated treatments. **J-M**: Representative images and relative quantification of C11 BODIPY staining and DHE staining in aged hLOs with indicated treatments (scale bar = 20 μm). Data are expressed as mean ± SD. *p < 0.05, **p < 0.01, ***p < 0.001, and ****p < 0.0001. MFI, mean fluorescence intensity. Ctr, control. IR, ischemia reperfusion. EVs, MSC-EVs. AAV, adeno-associated virus. oe, overexpression.

Therefore, in this study, we performed microarray analysis to characterize the miRNA expression profile of MSC-EVs. After three biological replicates, 35 miRNAs were found to be enriched in MSC-EVs (Fig. 7A). Using the TargetScan and MicroRNA Target Prediction Database (miRDB) databases, we predicted potential target genes for these miRNAs. This analysis suggested that miR-1275 could directly target SLC39A14 (Fig. 7B). FISH analysis revealed that miR-1275 was primarily localized in the cytoplasm of MSCs (Fig. 7C). To validate the direct interaction between miR-1275 and SLC39A14, we performed dual-luciferase reporter assays. The results demonstrated that overexpression or silenced of miR-1275 significantly influenced the luciferase activity of the reporter construct containing the wild-type SLC39A14 3′-UTR while having no effect on the luciferase activity of the reporter construct containing a mutated SLC39A14 3′-UTR. These findings suggested *SLC39A14* as a direct target gene of miR-1275 (Fig. 7D and Supplementary Figs. 13A–13B). In addition, treatment with MSC-EVs significantly increased the expression of miR-1275 in aged hepatocytes (Supplementary Fig. 14A). To validate the regulatory effect of miR-1275 on *SLC39A14*, aged hepatocytes were transfected with miR-1275 mimic and inhibitor. Following confirmation of transfection efficiency (Supplementary Figs. 14B–14C), we observed that the miR-1275 mimic significantly downregulated the expression of SLC39A14, whereas the miR-1275 inhibitor promoted its expression (Fig. 7E and Supplementary Figs. 14D–14E). To further confirm the binding between miR-1275 and SLC39A14, we performed RNA immunoprecipitation (RIP) assays. As shown in Supplementary Figs. 14F–14G, overexpressing miR-1275 could significantly elevate the recruitment of the *SLC39A14* mRNA to the miRNP complex, while silencing miR-1275 reversed, indicating a direct interaction between miR-1275 and SLC39A14. To investigate the functional significance of miR-1275 in MSC-EV-mediated protection, we isolated EVs from MSCs transfected with the miR-1275 inhibitor and subsequently added them to aged hepatocytes to compare their hepatoprotective role in the H/R model. Western blot analysis revealed that when miR-1275 expression in MSC-EVs was suppressed, the expression of SLC39A14 was significantly upregulated, accompanied by an increase in intracellular iron levels (Fig. 7F and Supplementary Figs. 15A–15B). Moreover, miR-1275 inhibition significantly weakened the anti-cell death effect of MSC-EVs (Fig. 7G–H) and blocked their potential to inhibit ferroptosis in the aged hepatocyte H/R model. This was evidenced by a reversal of the protective effects, as demonstrated by increased lipid peroxidation and ROS production, a higher abundance of mitochondria with reduced or disappeared cristae, and altered expression of ferroptosis-related proteins (Fig. 7I–L and Supplementary Figs. 15C–15E). Conversely, transfection of miR-1275 mimic into aged hepatocytes exerted a similar protective effect similar to that of MSC-EVs during H/R treatment, suggesting a potential role for miR-1275 in mediating the beneficial effects of MSC-EVs (Fig. 7G–L and Supplementary Figs. 15C–15E). Finally, we utilized the aged hLOs H/R model to confirm that the ability of MSC-EVs to suppress ferroptosis in aged hepatocytes during H/R treatment was dependent on miR-1275 (Fig. 7M–P).

3.7. MiR-1275 derived from MSC-EVs protects against ferroptosis and SLC39A14-related iron absorption in the aged HIRI model

Based on the *in vitro* findings, we further investigated the therapeutic potential of miR-1275 *in vivo*. We administered miR-1275 mimics or MSC-EVs derived from MSCs transfected with a miR-1275 inhibitor (MSC-EVs^{inhibitor}) to the aged HIRI model. The results demonstrated that miR-1275 mimics, similar to MSC-EVs, significantly attenuated liver injury in the aged HIRI model, evidenced by a reduction in serum levels of transaminases and an improvement in liver pathology, including a reduction in necrotic areas, disrupted hepatic lobules, and inflammatory cell infiltration (Fig. 8A–C and 8F-8G). Furthermore, miR-1275 mimics effectively limited ROS generation (Fig. 8D, 8H–8I, and Supplementary Figs. 16A–16B) and suppressed ferroptosis, as evidenced by alterations in the expression of ferroptosis-related proteins and reduced lipid peroxidation as assessed by C11 BODIPY staining (Fig. 8E, 8J-8K and Supplementary Fig. 16C). In contrast, MSC-EVs^{inhibitor} exhibited diminished protective effects against aged HIRI compared to MSC-EVs (Fig. 8A–K and Supplementary Figs. 16A–16C). To further elucidate the underlying mechanisms, we assessed the expression of SLC39A14 in liver tissues from each group. Compared to the control group, the miR-1275 mimics group exhibited significantly lower SLC39A14 expression. Moreover, the ability of MSC-EVs to reduce SLC39A14 expression was attenuated to some extent in the MSC-EVs^{inhibitor} group (Fig. 8L–M). Consistent with the changes in SLC39A14 expression, we observed that iron levels in liver tissues followed a similar trend across the five experimental groups (Fig. 8N–O). Collectively, these findings demonstrate that miR-1275 plays a crucial role in mediating the protective effects of MSC-EVs against aged HIRI by inhibiting ferroptosis.

4. Discussion

HIRI following transplantation with aged donor livers significantly impacts the prognosis of LT. However, due to a limited understanding of the underlying mechanisms, effective treatments for this patient population remain elusive. In this study, we provide hitherto undocumented evidence that MSC-EVs possess the capacity to attenuate aged HIRI. Our findings suggest that this protective effect was partly attributable to the ability of MSC-EVs to suppress iron accumulation in aged hepatocytes, thereby inhibiting ferroptosis. Furthermore, through comprehensive miRNA microarray analysis, we identified miR-1275 as a key component enriched within MSC-EVs. We provide compelling evidence that miR-1275 is transferred into aged hepatocytes and subsequently downregulates the expression of SLC39A14, a critical iron importer. Taken together, these findings suggest that MSC-EVs represent a promising nanotherapeutic approach for protecting aged liver grafts during LT.

Current evidence suggests that HIRI can induce severe programmed cell death in aged hepatocytes. Although interventions targeting hepatocellular apoptosis can partially mitigate aged HIRI, these approaches may not fully address the underlying mechanisms. Emerging evidence suggests that other forms of regulated cell death, such as ferroptosis, may also play a crucial role in the pathogenesis of aged HIRI [41,42]. Ferroptosis, a recently characterized form of iron-dependent, oxidative cell death, has been implicated in various liver diseases, including hepatocellular carcinoma [43], liver fibrosis [44], nonalcoholic fatty liver disease [45], sepsis-induced liver injury [46], and HIRI [47,48]. Aging is associated with increased susceptibility to ferroptosis due to factors such as intracellular iron overload, elevated ROS production, and dysregulated lipid metabolism. Previous studies from our research team have highlighted the significance of ferroptosis in aged HIRI, suggesting that therapeutic strategies targeting this pathway may offer a more effective approach to attenuating liver injury in the aging population [12]. However, currently available ferroptosis inhibitors are primarily in the preclinical stage of development, and their clinical translation remains uncertain. Therefore, the identification of alternative therapeutic approaches with high clinical translatability for regulating ferroptosis is of paramount importance. MSCs have emerged as a promising therapeutic option for various liver diseases due to their inherent regenerative, antioxidant, and immunomodulatory properties. Through previous clinical and experimental researches, we presented their benefits in liver injury and demonstrated that they adapted to the clinical utilisation of LT. A growing body of research has focused on MSC-EVs, as they are the major means for MSCs to perform biological functions. Our previous studies have demonstrated the hepatoprotective potential of MSC-EVs in HIRI and aged liver regeneration [19–22]. Given the complex and diverse nature of their cargo, MSC-EVs exert their biological functions through a variety of mechanisms. Several studies have reported the ability of MSC-EVs to inhibit ferroptosis in various disease models. In this respect, Wei Z et al. demonstrated that MSC-EVs could alleviate inflammatory bowel disease by inhibiting ferroptosis [25]. Lin F et al.

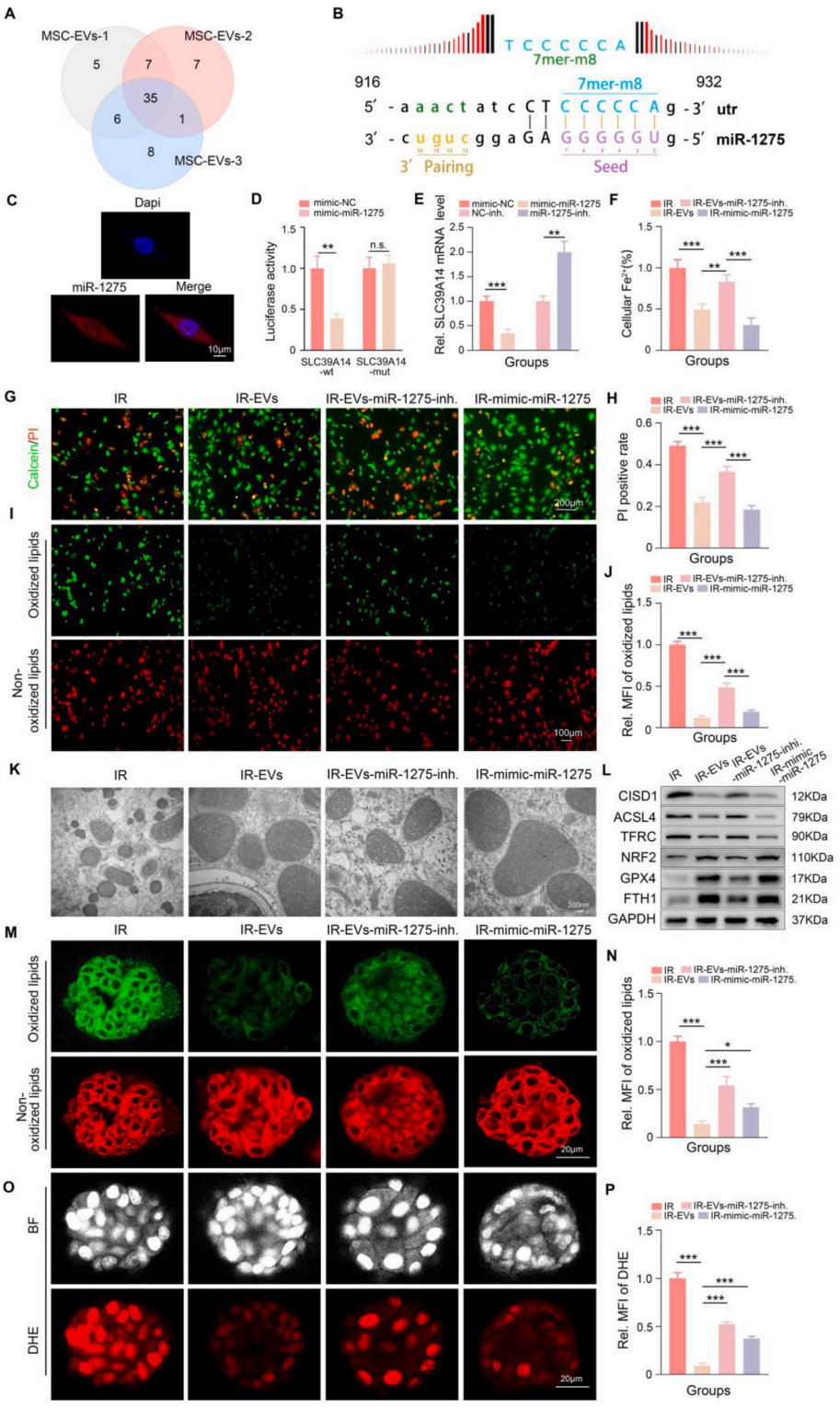

Fig. 7. MSC-EVs-derived miR-1275 downregulates SLC39A14 expression and mitigates ferroptosis. **A**: Microarray analysis of miRNA expression profiles of MSC-EVs with three biological replicates. **B**: Potential binding site of miR-1275 and SLC39A14 predicted by TargetScan and miRDB databases. **C**: Representative image of FISH assay image showing that miR-1275 is located in the cytoplasm of MSCs (scale bar = 10 μm). **D**: Dual luciferase reporter analysis showing the binding potential between miR-1275 and SLC39A14. **E**: Relative mRNA levels of SLC39A14 of aged hepatocytes treated by mimic miR-1275, mimic-NC, miR-1275 inhibitor and NC-inhibitor. For aged hepatocyte H/R model, **F**: Intracellular iron level in IR, IR-EVs, IR-EVs-miRNA-inhibitor, and IR-mimic-miR-1275 group. **G-J**: Representative images and relative quantification of Calcein-AM/PI double staining and C11 BODIPY staining of each group (scale bar = 200 μm). **K:** Representative TEM assays images showing the mitochondrial morphological characteristics in aged hepatocytes with indicated treatments (scale bar = 200 nm). **L**: Representative western blotting images showing the expression of ferroptosis-related proteins in each group. For aged hLOs H/R model, **M-P:** Representative images and relative quantification of C11 BODIPY staining and DHE staining in the IR, IR-EVs, IR-EVs-miRNA-inhibitor, and IR-mimic-miR-1275 groups (scale bar = 20 μm). Error bars represent the means of three independent experiments. Data are expressed as mean ± SD. *$p < 0.05$, **$p < 0.01$, ***$p < 0.001$, and ****$p < 0.0001$. MFI, mean fluorescence intensity. miR-1275, NC-inh, normal control-inhibitor. IR, ischemia reperfusion. EVs, MSC-EVs.

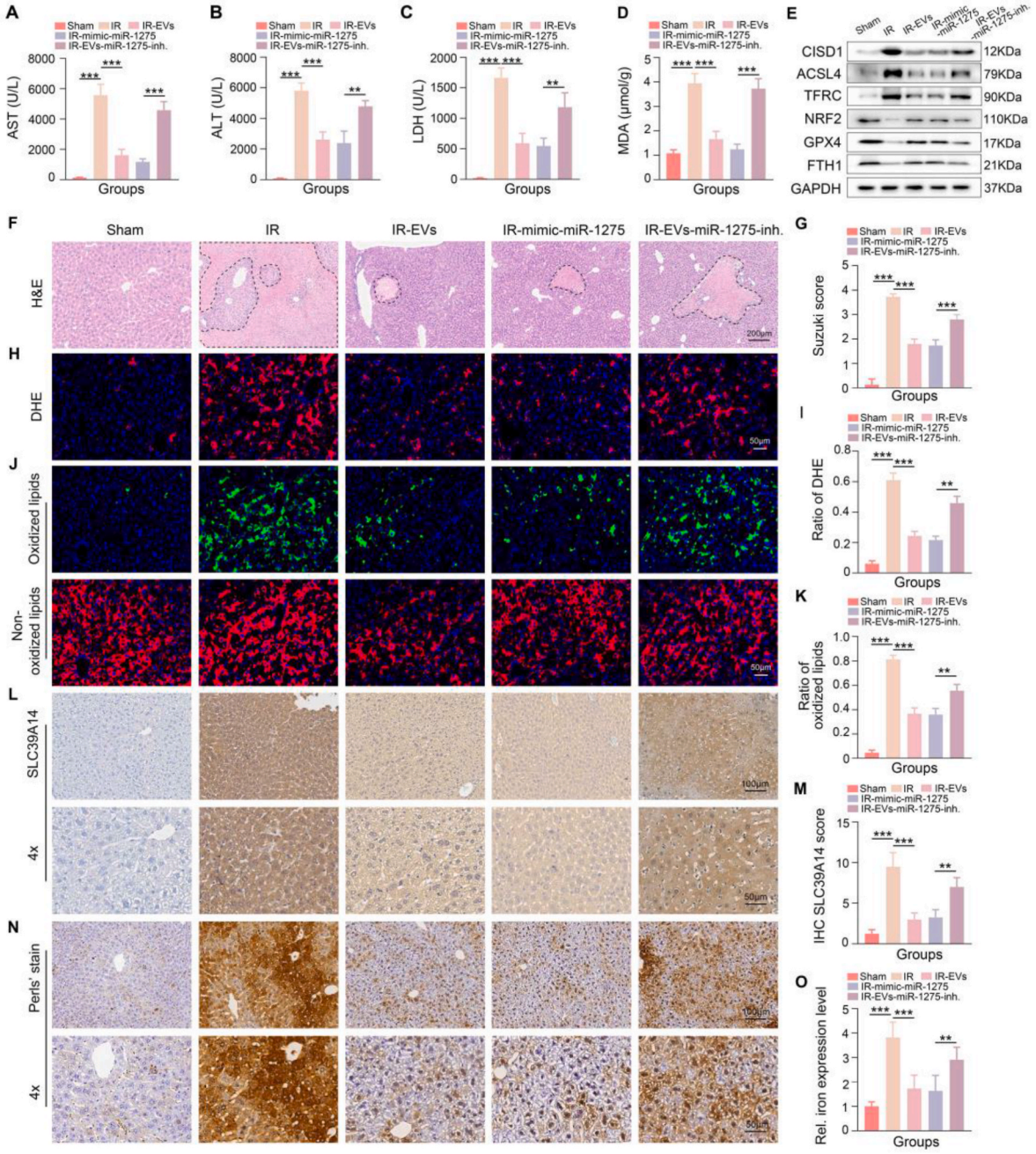

Fig. 8. miR-1275 derived from MSC-EVs could suppress ferroptosis and SLC39A14-related iron accumulation of the liver in aged HIRI model. **A-C:** The detection of serum levels of ALT, AST, and LDH in each group. **D:** MDA levels in each group. **E:** Representative western blotting image showing the expression of ferroptosis-related proteins in the five groups. **F–K:** Representative images and relative quantification of H&E staining (scale bar = 200 μm), DHE staining (scale bar = 50 μm), and C11 BODIPY staining (scale bar = 50 μm) of the five groups. **L-O:** Representative images and relative quantification of IHC about tissue SLC39A14 and iron levels of indicated groups (Up, scale bar = 100 μm, down, scale bar = 50 μm), (n = 3, per group). Data are expressed as mean ± SD. *p < 0.05, **p < 0.01, ***p < 0.001, and ****p < 0.0001. inh, inhibitor. IR, ischemia reperfusion. EVs, MSC-EVs.

reported that MSC-EVs could protect against ferroptosis in acute liver injury by regulating SLC7A11 stabilization [49]. Additionally, MSC-EVs have been shown to inhibit ferroptosis and ameliorate neuronal damage in spinal cord injury models by delivering circ-Wdfy3 [50]. However, whether MSC-EVs can regulate ferroptosis in other disease models and the underlying molecular mechanisms involved remain to be fully elucidated. In this study, our data provide substantial evidence that MSC-EVs can suppress ferroptosis and attenuate pathological injury in aged HIRI. Notably, co-administration with a ferroptosis activator significantly attenuated the hepatoprotective effects of MSC-EVs in the aged HIRI model.

Next, RNA-Seq was performed to elucidate the molecular mechanisms underlying the inhibitory effects of MSC-EVs on ferroptosis in aged hepatocytes during ischemia-reperfusion. RNA-Seq analysis revealed that ferroptosis-related signaling pathways were significantly upregulated in the PBS-treated group compared to the normal control group, while these pathways were suppressed in the MSC-EVs-treated group. Among these differentially expressed genes, *SLC39A14*, a critical iron ion importer, was significantly correlated with the observed changes in ferroptosis-related pathways. SLC39A14, a member of the SLC39A family of proteins, mediates the cellular uptake of non-transferrin-bound iron [51]. Previous studies on SLC39A14 mainly

focused on the role of iron transport disorders caused by the dysregulation of SLC39A14 in developmental or metabolism-related diseases [52,53]. Since the introduction of the concept of ferroptosis was introduced by Stockwell in 2012, key regulatory molecules involved in this unique form of regulated cell death have been identified, including SLC39A14. Fudi Wang et al. reported that silencing hepatic SLC39A14 expression can attenuate ferroptosis-mediated liver fibrosis induced by either a high-iron diet or carbon tetrachloride (CCl_4) injections [52]. Yierpani Aierken et al. reported that inhibition of SLC39A14 or SLC39A8 could mitigate vascular calcification by suppressing iron overload-induced ferroptosis in vascular smooth muscle cells [54]. Yunwen Zhang et al. proved that silencing SLC39A14 inhibits the progression of glioma by enhancing erastin-induced ferroptosis [55]. Furthermore, Hongyang Chi et al. showed that inhibition of SLC39A14 could alleviate ischemia-reperfusion injury in aging cardiomyocytes by regulating ferroptosis [56]. The present study demonstrated that SLC39A14 is highly expressed in aging livers and associated with more severe aged HIRI. We further demonstrated that this association is likely due to SLC39A14-mediated induction of cellular iron overload, leading to ferroptosis. While previous studies have explored the role of SLC39A14 in various physiological and pathological processes, effective therapeutic strategies for regulating its expression remain limited. This study provides novel evidence that MSC-EVs can effectively inhibit intrahepatocellular iron import and suppress ferroptosis in aged HIRI by downregulating SLC39A14 expression. Beyond SLC39A14, our findings suggest that MSC-EVs may also influence the expression of ferritin heavy chain 1 (FTH1). Previous studies have shown that FTH1 sequesters iron in a soluble, non-toxic, and readily available form, which reduces the level of free ferrous ions in cells and effectively decreases the occurrence of Fenton reaction, thereby inhibiting the ferroptosis [57–59]. These findings suggest that FTH1 may also contribute to the MSC-EV-mediated attenuation of aged HIRI by limiting iron accumulation. At present, there is a paucity of research on the role of FTH1 in aged HIRI, and whether MSC-EVs can directly regulate FTH1 expression remains unknown. These aspects warrant further investigation to fully elucidate the mechanisms underlying the hepatoprotective effects of MSC-EVs in aged HIRI.

MSC-EVs exert their biological functions primarily through their diverse cargo. Previous studies from our laboratory have demonstrated that MSC-EVs can attenuate HIRI through the delivery of various bioactive molecules, including MnSOD (for antioxidant defence), CCT2 (to inhibit CD154 expression on $CD4^+$ T cells), and functional mitochondria (to suppress the formation of neutrophil extracellular traps (NETs)). Furthermore, we have shown that MSC-EVs can enhance the regenerative potential of aged hepatocytes by transferring DDX5 [19–22]. miRNAs, a class of non-coding, single-stranded RNA molecules, primarily regulate gene expression at the post-transcriptional level. Emerging evidence suggests that miRNAs are crucial components of MSC-EVs and play a significant role in mediating their effects on recipient cells. Therefore, we conducted a miRNA microarray analysis to screen out the MSC-EVs-enriched miRNAs and found that miRNAs in MSC-EVs had a significant affection to suppress iron accumulation in aged hepatocytes during H/R treatment. Among the identified miRNAs, miR-1275 was found to be enriched in MSC-EVs and exhibited potential protective effects in aged hepatocytes. Further experiments utilizing miR-1275 mimics and inhibitors confirmed these findings. MiR-1275 mimics effectively inhibited iron import and suppressed ferroptosis in aged hepatocytes during IR injury, whereas miR-1275 inhibitors significantly attenuated the protective effects of MSC-EVs in this model. Previous studies on miR-1275 have primarily focused on its role in cancer progression. For example, Zheng ZQ et al. demonstrated that miR-1275 inhibits tumorigenesis and metastasis of nasopharyngeal carcinoma through downregulation of integrin β3 (ITGB3) [60]. Han X et al. reported that miR-1275 suppressed chemoresistance in breast cancer by targeting the MDK/AKT signaling pathway, thereby mitigating cancer stem cell characteristics [61]. MiR-1275 has also been shown to play roles in enhancing the stemness, tumorigenicity, recurrence, and metastasis of lung adenocarcinoma by activating the Wnt/β-catenin and Notch signaling pathways [62]. Additionally, miR-1275 can induce cisplatin resistance in lung cancer cells by targeting the PROCA1/ZFP36L2 axis [63]. Interestingly, recent studies have begun to explore the functions of miR-1275 in benign diseases. Notably, miR-1275 has been demonstrated to alleviate myocardial ischemia-reperfusion injury (IRI) by inhibiting myocyte apoptosis [64,65]. These findings suggest a broader role for miR-1275 beyond cancer biology. In this study, we utilized miRTarBase (http://miRTarBase.cuhk.edu.cn/) to identify potential targets of miR-1275. We found that SLC39A14, a critical iron importer, is an experimentally validated target of miR-1275. This suggests that miR-1275 may represent a novel therapeutic target for protecting aged grafts during LT by inhibiting iron accumulation and ferroptosis in aged hepatocytes.

In conclusion, this study demonstrates the novel therapeutic potential of MSC-EVs in attenuating aged HIRI. Mechanistically, our findings suggest that MSC-EVs exert their protective effects, at least in part, through the delivery of miR-1275. By suppressing the expression of SLC39A14, miR-1275 within MSC-EVs effectively limits iron accumulation and inhibits ferroptosis in aged hepatocytes (Fig. 9). These findings further underscore the bioactive capabilities of MSC-EVs in inhibiting ferroptosis and alleviating aged HIRI. Therefore, MSC-EVs may represent an attractive therapeutic strategy for improving the prognosis and preventing serious complications in recipients of aged liver grafts following LT.

CRediT authorship contribution statement

Yihang Gong: Writing – original draft, Validation, Methodology, Data curation, Conceptualization. **Qiang You:** Writing – review & editing, Writing – original draft, Methodology, Data curation, Conceptualization. **Xiaofeng Yuan:** Visualization, Supervision, Methodology, Conceptualization. **Fanxin Zeng:** Methodology, Investigation, Data curation. **Feng Zhang:** Software, Conceptualization. **Jiaqi Xiao:** Methodology, Investigation. **Haitian Chen:** Visualization, Conceptualization. **Yasong Liu:** Investigation, Formal analysis, Conceptualization. **Tingting Wang:** Investigation, Data curation, Conceptualization. **Xijing Yan:** Methodology. **Wenjie Chen:** Supervision, Data curation, Conceptualization. **Yingcai Zhang:** Investigation, Funding acquisition, Formal analysis. **Qi Zhang:** Supervision. **Jia Yao:** Investigation, Funding acquisition, Conceptualization. **Jiebin Zhang:** Investigation, Funding acquisition, Conceptualization. **Rong Li:** Writing – review & editing, Writing – original draft, Validation, Supervision, Funding acquisition, Data curation. **Jun Zheng:** Writing – original draft, Visualization, Supervision.

Data availability statement

The data that support the findings of this study are available from the corresponding author upon reasonable request.

Funding

This work was supported by the grants from the National Key Research and Development Program of China (2024YFA1107200, 2022YFA1104903); the National Natural Science Foundation of China (82470666, 82303474, 81802897, 82270689, 82300747, 82400742); Natural Science Foundation of Guangdong Province (2024A1515010701, 2021A1515012136, 2021A1515011156, 2021A1515010571, 2023A1515030052, 2023A1515010346, 2024A1515011662), China Postdoctoral Science Foundation (2022M720176, 2024T171075), Postdoctoral Fellowship Program of CPSF, Guangdong Basic and Applied Basic Research Foundation (2021A1515111058); Guangzhou Basic and Applied Basic Research Project Co-funded by Municipal Schools (institutes) (2024A03J0273,

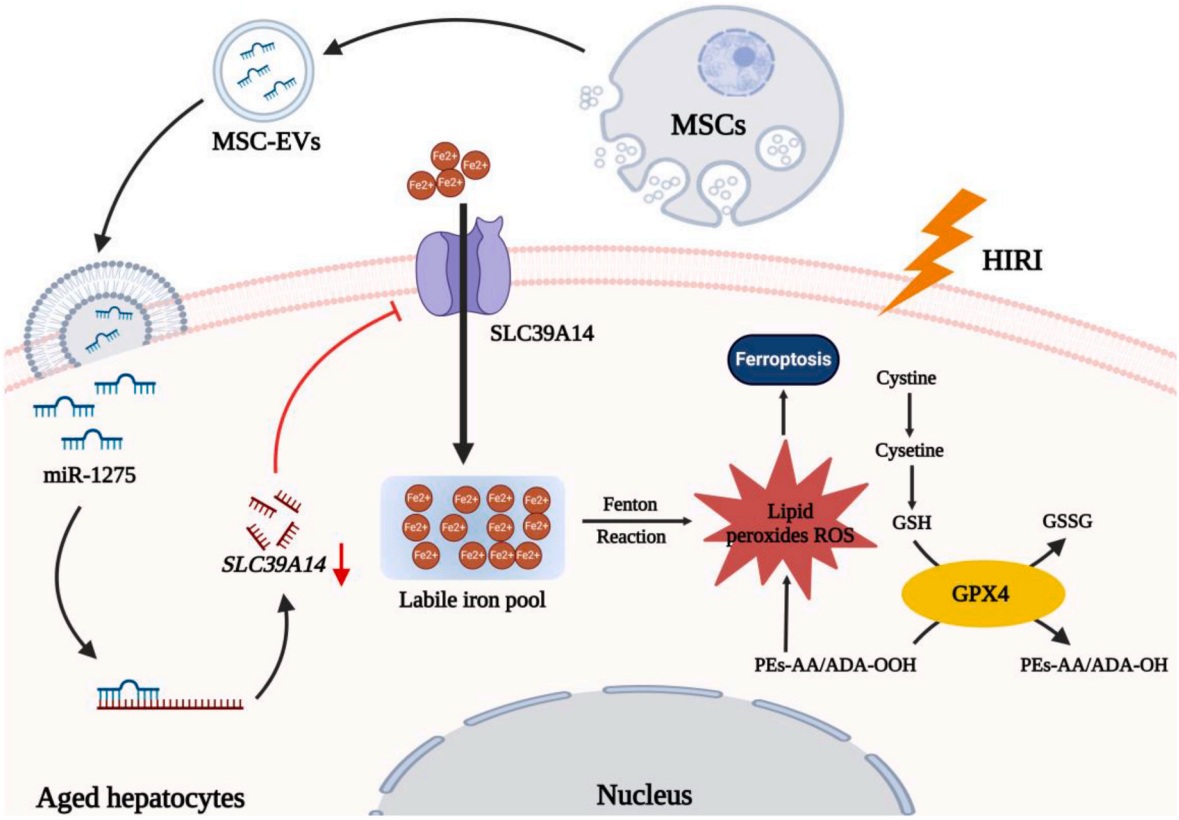

Fig. 9. MiR-1275 in MSC-EVs suppresses the expression of SLC39A14 and subsequently limits iron accumulation to inhibit ferroptosis of aged hepatocytes to alleviate aged hepatic ischemia/reperfusion injury.

2023A03J0727, 2023A1515010346), Guangzhou Basic and Applied Basic Research Key Foundation (2024B03J1382), Guangzhou Basic and Applied Basic Research Foundation (202102020237, 202201010815), Major talent project cultivation plan project of 3rd Affiliated Hospital of SYSU (P02093, P02454), Academician Shusen Lanjuan Talent foundation (Yingcai Zhang, Jun Zheng), Liver Transplantation Program of People's Hospital of Xinjiang Uyghur Autonomous Region (20240101), Youth Enhancement Project of Guangdong Provincial Natural Science Foundation (2023A1515030052).

Declaration of competing interest

The authors declare that they have no known competing financial interests or personal relationships that could have appeared to influence the work reported in this paper.

Acknowledgement

None.

Abbreviation

HIRI, hepatic ischemia/reperfusion injury; LT, liver transplantation; MSCs, mesenchymal stem cells; MSC-EVs, mesenchymal stem cell-derived extracellular vesicles; miR-1275, nicroRNA-1275; TFRC, transferrin receptor protein 1. TMEM16A, transmembrane member 16A; GPX4, glutathione peroxidation 4; FTO, fat mass and obesity-associated gene; ACSL4, acyl-CoA synthetase long chain family 4; FTH1, ferritin heavy chain 1; GPX4, glutathione peroxidase 4; NRF2, NF-E2-related factor-2; BF, bright field; PBS, phosphate buffer saline; UCs, umbilical cords; DMEM, Dulbecco's modified Eagle's medium; FBS, fetal bovine serum; BCA, bicinchoninic acid; TEM, Transmission electron microscope; NTA, nanoparticle tracking analysis; ALT, serum alanine aminotransferase; AST, aspartate aminotransferase; POD, postoperative day; SPF, specific pathogen-free; LDH, lactate dehydrogenase; PFA, paraformaldehyde; H&E, hematoxylin and eosin; RIPA, radioimmunoprecipitation; SDS, sodium dodecyl sulfate; EDTA, ethylene diamine tetraacetic acid; PAGE, polyacrylamide gel electrophoresis; PVDF, polyvinylidene difluoride; MDA, malondialdehyde; SOD, superoxide; GSH, glutathione; DHE, Dihydroethidium dye; AAV8, Adeno-associated virus-8; GFP, green fluorescent protein gene; hLOs, human liver organoids; β-gal, β-galactosidase; H/R, hypoxia reoxygenation; IF, Immunofluorescence; ANOVA, analysis of variance; MSCs-CM, MSCs-conditioned medium; GRP94, glucose-regulated protein 94; HNF-4α, hepatocyte nuclear factor 4α; ALB, Albumin; LGR5, Leucine-rich repeat-containing G-protein coupled receptor 5; NETs, neutrophil extracellular traps; ITGB3, integrin β3.

Appendix A. Supplementary data

Supplementary data to this article can be found online at https://doi.org/10.1016/j.redox.2025.103556.

Data availability

Data will be made available on request.

References

[1] K.M. Dickson, P.N. Martins, Implications of liver donor age on ischemia reperfusion injury and clinical outcomes, Transplant. Rev. 34 (3) (2020) 100549.
[2] D. Wu, L. Liu, N. Jiao, Y. Zhang, L. Yang, C. Tian, P. Lan, L. Zhu, R. Loomba, R. Zhu, Targeting keystone species helps restore the dysbiosis of butyrate-producing bacteria in nonalcoholic fatty liver disease, Imeta 1 (4) (2022) e61.
[3] F. Durand, J. Levitsky, F. Cauchy, H. Gilgenkrantz, O. Soubrane, C. Francoz, Age and liver transplantation, J. Hepatol. 70 (4) (2019) 745–758.

[4] X. Chen, R. Kang, G. Kroemer, D. Tang, Ferroptosis in infection, inflammation, and immunity, J. Exp. Med. 218 (6) (2021).
[5] Y. Meng, H.-Y. Sun, Y. He, Q. Zhou, Y.-H. Liu, H. Su, M.-Z. Yin, F.-R. Zeng, X. Chen, G.-T. Deng, BET inhibitors potentiate melanoma ferroptosis and immunotherapy through AKR1C2 inhibition, Mil Med Res 10 (1) (2023) 61.
[6] J. Chen, X. Li, C. Ge, J. Min, F. Wang, The multifaceted role of ferroptosis in liver disease, Cell Death Differ. 29 (3) (2022) 467–480.
[7] C. Conche, F. Finkelmeier, M. Pešić, A.M. Nicolas, T.W. Böttger, K.B. Kennel, D. Denk, F. Ceteci, K. Mohs, E. Engel, Ö. Canli, Y. Dabiri, K.-H. Peiffer, S. Zeuzem, G. Salinas, T. Longerich, H. Yang, F.R. Greten, Combining ferroptosis induction with MDSC blockade renders primary tumours and metastases in liver sensitive to immune checkpoint blockade, Gut 72 (9) (2023) 1774–1782.
[8] Q.-Q. Zhang, Q. Chen, P. Cao, C.-X. Shi, L.-Y. Zhang, L.-W. Wang, Z.-J. Gong, AGK2 pre-treatment protects against thioacetamide-induced acute liver failure via regulating the MFN2-PERK axis and ferroptosis signaling pathway, Hepatobiliary Pancreat. Dis. Int. 23 (1) (2024) 43–51.
[9] N. Yamada, T. Karasawa, T. Wakiya, A. Sadatomo, H. Ito, R. Kamata, S. Watanabe, T. Komada, H. Kimura, Y. Sanada, Y. Sakuma, K. Mizuta, N. Ohno, N. Sata, M. Takahashi, Iron overload as a risk factor for hepatic ischemia-reperfusion injury in liver transplantation: potential role of ferroptosis, Am. J. Transplant. 20 (6) (2020) 1606–1618.
[10] Y. Wu, H. Jiao, Y. Yue, K. He, Y. Jin, J. Zhang, J. Zhang, Y. Wei, H. Luo, Z. Hao, X. Zhao, Q. Xia, Q. Zhong, J. Zhang, Ubiquitin ligase E3 HUWE1/MULE targets transferrin receptor for degradation and suppresses ferroptosis in acute liver injury, Cell Death Differ. 29 (9) (2022) 1705–1718.
[11] J. Guo, Z. Song, J. Yu, C. Li, C. Jin, W. Duan, X. Liu, Y. Liu, S. Huang, Y. Tuo, F. Pei, Z. Jian, P. Zhou, S. Zheng, Z. Zou, F. Zhang, Q. Gong, S. Liang, Hepatocyte-specific TMEM16A deficiency alleviates hepatic ischemia/reperfusion injury via suppressing GPX4-mediated ferroptosis, Cell Death Dis. 13 (12) (2022) 1072.
[12] R. Li, X. Yan, C. Xiao, T. Wang, X. Li, Z. Hu, J. Liang, J. Zhang, J. Cai, X. Sui, Q. Liu, M. Wu, J. Xiao, H. Chen, Y. Liu, C. Jiang, G. Lv, G. Chen, Y. Zhang, J. Yao, J. Zheng, Y. Yang, FTO deficiency in older livers exacerbates ferroptosis during ischaemia/reperfusion injury by upregulating ACSL4 and TFRC, Nat. Commun. 15 (1) (2024) 4760.
[13] J. Zheng, L. Chen, T. Lu, Y. Zhang, X. Sui, Y. Li, X. Huang, L. He, J. Cai, C. Zhou, J. Liang, G. Chen, J. Yao, Y. Yang, MSCs ameliorate hepatocellular apoptosis mediated by PINK1-dependent mitophagy in liver ischemia/reperfusion injury through AMPKα activation, Cell Death Dis. 11 (4) (2020) 256.
[14] S. Li, X. Zheng, H. Li, J. Zheng, X. Chen, W. Liu, Y. Tai, Y. Zhang, G. Wang, Y. Yang, Mesenchymal stem cells ameliorate hepatic ischemia/reperfusion injury via inhibition of neutrophil recruitment, J Immunol Res 2018 (2018) 7283703.
[15] J. Zheng, H. Li, L. He, Y. Huang, J. Cai, L. Chen, C. Zhou, H. Fu, T. Lu, Y. Zhang, J. Yao, Y. Yang, Preconditioning of umbilical cord-derived mesenchymal stem cells by rapamycin increases cell migration and ameliorates liver ischaemia/reperfusion injury in mice via the CXCR4/CXCL12 axis, Cell Prolif. 52 (2) (2019) e12546.
[16] Y. Zhang, J. Zhang, H. Yi, J. Zheng, J. Cai, W. Chen, T. Lu, L. Chen, C. Du, J. Liu, J. Yao, H. Zhao, G. Wang, B. Fu, T. Zhang, J. Zhang, G. Wang, H. Li, A.P. Xiang, G. Chen, S. Yi, Q. Zhang, Y. Yang, A novel MSC-based immune induction strategy for ABO-incompatible liver transplantation: a phase I/II randomized, open-label, controlled trial, Stem Cell Res. Ther. 12 (1) (2021) 244.
[17] Y.-C. Zhang, W. Liu, B.-S. Fu, G.-Y. Wang, H.-B. Li, H.-M. Yi, N. Jiang, G. Wang, J. Zhang, S.-H. Yi, H. Li, Q. Zhang, Y. Yang, G.-H. Chen, Therapeutic potentials of umbilical cord-derived mesenchymal stromal cells for ischemic-type biliary lesions following liver transplantation, Cytotherapy 19 (2) (2017) 194–199.
[18] S.R. Baglio, D.M. Pegtel, N. Baldini, Mesenchymal stem cell secreted vesicles provide novel opportunities in (stem) cell-free therapy, Front. Physiol. 3 (2012) 359.
[19] J. Yao, J. Zheng, J. Cai, K. Zeng, C. Zhou, J. Zhang, S. Li, H. Li, L. Chen, L. He, H. Chen, H. Fu, Q. Zhang, G. Chen, Y. Yang, Y. Zhang, Extracellular vesicles derived from human umbilical cord mesenchymal stem cells alleviate rat hepatic ischemia-reperfusion injury by suppressing oxidative stress and neutrophil inflammatory response, FASEB J. 33 (2) (2019) 1695–1710.
[20] J. Zheng, T. Lu, C. Zhou, J. Cai, X. Zhang, J. Liang, X. Sui, X. Chen, L. Chen, Y. Sun, J. Zhang, W. Chen, Y. Zhang, J. Yao, G. Chen, Y. Yang, Extracellular vesicles derived from human umbilical cord mesenchymal stem cells protect liver ischemia/reperfusion injury by reducing CD154 expression on CD4+ T cells via CCT2, Adv. Sci. 7 (18) (2020) 1903746.
[21] T. Lu, J. Zhang, J. Cai, J. Xiao, X. Sui, X. Yuan, R. Li, Y. Li, J. Yao, G. Lv, X. Chen, H. Chen, K. Zeng, Y. Liu, W. Chen, G. Chen, Y. Yang, J. Zheng, Y. Zhang, Extracellular vesicles derived from mesenchymal stromal cells as nanotherapeutics for liver ischaemia-reperfusion injury by transferring mitochondria to modulate the formation of neutrophil extracellular traps, Biomaterials 284 (2022) 121486.
[22] H. Chen, W. Yin, K. Yao, J. Liang, J. Cai, X. Sui, X. Zhao, J. Zhang, J. Xiao, R. Li, Q. Liu, J. Yao, G. You, Y. Liu, C. Jiang, X. Qiu, T. Wang, Q. You, Y. Zhang, M. Yang, J. Zheng, Z. Dai, Y. Yang, Mesenchymal stem cell membrane-camouflaged liposomes for biomimetic delivery of cyclosporine A for hepatic ischemia-reperfusion injury prevention, Adv. Sci. 11 (32) (2024) e2404171.
[23] J. Zhang, T. Lu, J. Xiao, C. Du, H. Chen, R. Li, X. Sui, Z. Pan, C. Xiao, X. Zhao, J. Yao, Y. Liu, Y. Lei, Y. Ruan, J. Zhang, H. Li, Q. Zhang, Y. Zhang, J. Cai, Y. Yang, J. Zheng, MSC-derived extracellular vesicles as nanotherapeutics for promoting aged liver regeneration, J Control Release 356 (2023) 402–415.
[24] L. Chen, Y. Liu, Z. Wang, L. Zhang, Y. Xu, Y. Li, L. Zhang, G. Wang, S. Yang, G. Xue, Mesenchymal stem cell-derived extracellular vesicles protect against abdominal aortic aneurysm formation by inhibiting NET-induced ferroptosis, Exp. Mol. Med. 55 (5) (2023) 939–951.
[25] Z. Wei, S. Hang, D.K. Wiredu Ocansey, Z. Zhang, B. Wang, X. Zhang, F. Mao, Human umbilical cord mesenchymal stem cells derived exosome shuttling mir-129-5p attenuates inflammatory bowel disease by inhibiting ferroptosis, J Nanobiotechnology 21 (1) (2023) 188.
[26] C. Shao, Y. Chen, T. Yang, H. Zhao, D. Li, Mesenchymal stem cell derived exosomes suppress neuronal cell ferroptosis via lncGm36569/miR-5627-5p/FSP1 Axis in acute spinal cord injury, Stem Cell Rev Rep 18 (3) (2022) 1127–1142.
[27] J.-Y. Ding, M.-J. Chen, L.-F. Wu, G.-F. Shu, S.-J. Fang, Z.-Y. Li, X.-R. Chu, X.-K. Li, Z.-G. Wang, J.-S. Ji, Mesenchymal stem cell-derived extracellular vesicles in skin wound healing: roles, opportunities and challenges, Mil Med Res 10 (1) (2023) 36.
[28] R. Adam, V. Delvart, V. Karam, C. Ducerf, F. Navarro, C. Letoublon, J. Belghiti, D. Pezet, D. Castaing, Y.P. Le Treut, J. Gugenheim, P. Bachellier, J. Pirenne, P. Muiesan, Compared efficacy of preservation solutions in liver transplantation: a long-term graft outcome study from the European Liver Transplant Registry, Am. J. Transplant. 15 (2) (2015) 395–406.
[29] Z.A. Stewart, UW solution: still the "gold standard" for liver transplantation, Am. J. Transplant. 15 (2) (2015) 295–296.
[30] J. Zheng, X. Yan, T. Lu, W. Song, Y. Li, J. Liang, J. Zhang, J. Cai, X. Sui, J. Xiao, H. Chen, G. Chen, Q. Zhang, Y. Liu, Y. Yang, K. Zheng, Z. Pan, CircFOXK2 promotes hepatocellular carcinoma progression and leads to a poor clinical prognosis via regulating the Warburg effect, J. Exp. Clin. Cancer Res. 42 (1) (2023) 63.
[31] L.P. Tan, E. Seinen, G. Duns, D. de Jong, O.C.M. Sibon, S. Poppema, B.-J. Kroesen, K. Kok, A. van den Berg, A high throughput experimental approach to identify miRNA targets in human cells, Nucleic Acids Res. 37 (20) (2009) e137.
[32] W.S. Yang, R. SriRamaratnam, M.E. Welsch, K. Shimada, R. Skouta, V. S. Viswanathan, J.H. Cheah, P.A. Clemons, A.F. Shamji, C.B. Clish, L.M. Brown, A. W. Girotti, V.W. Cornish, S.L. Schreiber, B.R. Stockwell, Regulation of ferroptotic cancer cell death by GPX4, Cell 156 (1–2) (2014) 317–331.
[33] I. Costa, D.J. Barbosa, S. Benfeito, V. Silva, D. Chavarria, F. Borges, F. Remião, R. Silva, Molecular mechanisms of ferroptosis and their involvement in brain diseases, Pharmacol. Ther. 244 (2023) 108373.
[34] S. Doll, B. Proneth, Y.Y. Tyurina, E. Panzilius, S. Kobayashi, I. Ingold, M. Irmler, J. Beckers, M. Aichler, A. Walch, H. Prokisch, D. Trümbach, G. Mao, F. Qu, H. Bayir, J. Füllekrug, C.H. Scheel, W. Wurst, J.A. Schick, V.E. Kagan, J.P.F. Angeli, M. Conrad, ACSL4 dictates ferroptosis sensitivity by shaping cellular lipid composition, Nat. Chem. Biol. 13 (1) (2017) 91–98.
[35] L. Su, J. Zhang, H. Gomez, J.A. Kellum, Z. Peng, Mitochondria ROS and mitophagy in acute kidney injury, Autophagy 19 (2) (2023) 401–414.
[36] M. Gao, P. Monian, Q. Pan, W. Zhang, J. Xiang, X. Jiang, Ferroptosis is an autophagic cell death process, Cell Res. 26 (9) (2016) 1021–1032.
[37] Z. Zhang, M. Guo, Y. Li, M. Shen, D. Kong, J. Shao, H. Ding, S. Tan, A. Chen, F. Zhang, S. Zheng, RNA-binding protein ZFP36/TTP protects against ferroptosis by regulating autophagy signaling pathway in hepatic stellate cells, Autophagy 16 (8) (2020) 1482–1505.
[38] Y. Jin, S. Cai, Y. Zhou, D. Guo, Y. Zeng, W. Xu, Y. Sun, Y. Shi, Z. Xu, Z. Liu, P. Luo, Z. Huang, B. Tang, Targeting SLC7A11/xCT improves radiofrequency ablation efficacy of HCC by dendritic cells mediated anti-tumor immune response, Imeta 3 (6) (2024) e248.
[39] V.V.T. Nguyen, S. Ye, V. Gkouzioti, M.E. van Wolferen, F.Y. Yengej, D. Melkert, S. Siti, B. de Jong, P.J. Besseling, B. Spee, L.J.W. van der Laan, R. Horland, M. C. Verhaar, B.W.M. van Balkom, A human kidney and liver organoid-based multi-organ-on-a-chip model to study the therapeutic effects and biodistribution of mesenchymal stromal cell-derived extracellular vesicles, J. Extracell. Vesicles 11 (11) (2022) e12280.
[40] S. Jenkitkasemwong, C.-Y. Wang, R. Coffey, W. Zhang, A. Chan, T. Biel, J.-S. Kim, S. Hojyo, T. Fukada, M.D. Knutson, SLC39A14 is required for the development of hepatocellular iron overload in murine models of hereditary hemochromatosis, Cell Metab. 22 (1) (2015) 138–150.
[41] S.K. Chun, S. Lee, J. Flores-Toro, R.Y. U, M.-J. Yang, K.L. Go, T.G. Biel, C.E. Miney, S. Pierre Louis, B.K. Law, M.E. Law, E.M. Thomas, K.E. Behrns, C. Leeuwenburgh, J.-S. Kim, Loss of sirtuin 1 and mitofusin 2 contributes to enhanced ischemia/reperfusion injury in aged livers, Aging Cell 17 (4) (2018) e12761.
[42] W. Zhong, Z. Rao, J. Rao, G. Han, P. Wang, T. Jiang, X. Pan, S. Zhou, H. Zhou, X. Wang, Aging aggravated liver ischemia and reperfusion injury by promoting STING-mediated NLRP3 activation in macrophages, Aging Cell 19 (8) (2020) e13186.
[43] X. Hao, Z. Zheng, H. Liu, Y. Zhang, J. Kang, X. Kong, D. Rong, G. Sun, G. Sun, L. Liu, H. Yu, W. Tang, X. Wang, Inhibition of APOC1 promotes the transformation of M2 into M1 macrophages via the ferroptosis pathway and enhances anti-PD1 immunotherapy in hepatocellular carcinoma based on single-cell RNA sequencing, Redox Biol. 56 (2022) 102463.
[44] Y. Fu, X. Zhou, L. Wang, W. Fan, S. Gao, D. Zhang, Z. Ling, Y. Zhang, L. Ma, F. Bai, J. Chen, B. Sun, P. Liu, Salvianolic acid B attenuates liver fibrosis by targeting Ecm1 and inhibiting hepatocyte ferroptosis, Redox Biol. 69 (2024) 103029.
[45] T. Jiang, Y. Xiao, J. Zhou, Z. Luo, L. Yu, Q. Liao, S. Liu, X. Qi, H. Zhang, M. Hou, W. Miao, B. Batsaikhan, T. Damba, Y. Liang, Y. Li, L. Zhou, Arbutin alleviates fatty liver by inhibiting ferroptosis via FTO/SLC7A11 pathway, Redox Biol. 68 (2023) 102963.
[46] L. Xie, C. Zhou, Y. Wu, X. Fu, G. Zhang, X. Han, S. Xie, G. Chen, H. Xu, B. Deng, B. Liu, Y. Zhou, A. Li, Wenqingyin suppresses ferroptosis in the pathogenesis of sepsis-induced liver injury by activating the Nrf2-mediated signaling pathway, Phytomedicine 114 (2023) 154748.
[47] C. Li, Y. Wu, K. Chen, R. Chen, S. Xu, B. Yang, Z. Lian, X. Wang, K. Wang, H. Xie, S. Zheng, Z. Liu, D. Wang, X. Xu, Gp78 deficiency in hepatocytes alleviates hepatic ischemia-reperfusion injury via suppressing ACSL4-mediated ferroptosis, Cell Death Dis. 14 (12) (2023) 810.

[48] X. Fang, J. Zhang, Y. Li, Y. Song, Y. Yu, Z. Cai, F. Lian, J. Yang, J. Min, F. Wang, Malic enzyme 1 as a novel anti-ferroptotic regulator in hepatic ischemia/reperfusion injury, Adv. Sci. 10 (13) (2023) e2205436.
[49] F. Lin, W. Chen, J. Zhou, J. Zhu, Q. Yao, B. Feng, X. Feng, X. Shi, Q. Pan, J. Yu, L. Li, H. Cao, Mesenchymal stem cells protect against ferroptosis via exosome-mediated stabilization of SLC7A11 in acute liver injury, Cell Death Dis. 13 (3) (2022) 271.
[50] M. Shao, S. Ye, Y. Chen, C. Yu, W. Zhu, Exosomes from hypoxic ADSCs ameliorate neuronal damage post spinal cord injury through circ-Wdfy3 delivery and inhibition of ferroptosis, Neurochem. Int. 177 (2024) 105759.
[51] S. Jenkitkasemwong, A. Akinyode, E. Paulus, R. Weiskirchen, S. Hojyo, T. Fukada, G. Giraldo, J. Schrier, A. Garcia, C. Janus, B. Giasson, M.D. Knutson, SLC39A14 deficiency alters manganese homeostasis and excretion resulting in brain manganese accumulation and motor deficits in mice, Proc. Natl. Acad. Sci. U. S. A. 115 (8) (2018) E1769–E1778.
[52] Y. Yu, L. Jiang, H. Wang, Z. Shen, Q. Cheng, P. Zhang, J. Wang, Q. Wu, X. Fang, L. Duan, S. Wang, K. Wang, P. An, T. Shao, R.T. Chung, S. Zheng, J. Min, F. Wang, Hepatic transferrin plays a role in systemic iron homeostasis and liver ferroptosis, Blood 136 (6) (2020) 726–739.
[53] A.N. Rodichkin, T.R. Guilarte, Hereditary disorders of manganese metabolism: pathophysiology of childhood-onset dystonia-parkinsonism in SLC39A14 mutation carriers and genetic animal models, Int. J. Mol. Sci. 23 (21) (2022).
[54] Y. Aierken, H. He, R. Li, Z. Lin, T. Xu, L. Zhang, Y. Wu, Y. Liu, Inhibition of Slc39a14/Slc39a8 reduce vascular calcification via alleviating iron overload induced ferroptosis in vascular smooth muscle cells, Cardiovasc. Diabetol. 23 (1) (2024) 186.
[55] Y. Zhang, X. Wu, J. Zhu, R. Lu, Y. Ouyang, Knockdown of SLC39A14 inhibits glioma progression by promoting erastin-induced ferroptosis SLC39A14 knockdown inhibits glioma progression, BMC Cancer 23 (1) (2023) 1120.
[56] H. Chi, Y.e. Chai, L. Ma, Y. Wang, Q. Wu, L. Wang, J. Zhai, F. Ma, Y. Tian, N. Qi, J. Peng, Y. Fu, X. Yang, H. Huang, S. Ma, The mechanism by which piR-000699 targets SLC39A14 regulates ferroptosis in aging myocardial ischemia/reperfusion injury, Acta Biochim. Biophys. Sin. 2024 Mar 4;56(9):1352-1364. .
[57] X.-Y. Zhang, S.-S. Li, Y.-R. Gu, L.-X. Xiao, X.-Y. Ma, X.-R. Chen, J.-L. Wang, C.-H. Liao, B.-L. Lin, Y.-H. Huang, Y.-F. Lian, CircPIAS1 promotes hepatocellular carcinoma progression by inhibiting ferroptosis via the miR-455-3p/NUPR1/FTH1 axis, Mol. Cancer 23 (1) (2024) 113.
[58] R. Zhang, T. Pan, Y. Xiang, M. Zhang, H. Xie, Z. Liang, B. Chen, C. Xu, J. Wang, X. Huang, Q. Zhu, Z. Zhao, Q. Gao, C. Wen, W. Liu, W. Ma, J. Feng, X. Sun, T. Duan, E. Lai-Han Leung, T. Xie, Q. Wu, X. Sui, Curcumenol triggered ferroptosis in lung cancer cells via lncRNA H19/miR-19b-3p/FTH1 axis, Bioact. Mater. 13 (2022) 23–36.
[59] N. Kong, X. Chen, J. Feng, T. Duan, S. Liu, X. Sun, P. Chen, T. Pan, L. Yan, T. Jin, Y. Xiang, Q. Gao, C. Wen, W. Ma, W. Liu, M. Zhang, Z. Yang, W. Wang, R. Zhang, B. Chen, T. Xie, X. Sui, W. Tao, Baicalin induces ferroptosis in bladder cancer cells by downregulating FTH1, Acta Pharm. Sin. B 11 (12) (2021) 4045–4054.
[60] Z.-Q. Zheng, Z.-X. Li, G.-Q. Zhou, L. Lin, L.-L. Zhang, J.-W. Lv, X.-D. Huang, R.-Q. Liu, F. Chen, X.-J. He, J. Kou, J. Zhang, X. Wen, Y.-Q. Li, J. Ma, N. Liu, Y. Sun, Long noncoding RNA FAM225A promotes nasopharyngeal carcinoma tumorigenesis and metastasis by acting as ceRNA to sponge miR-590-3p/miR-1275 and upregulate ITGB3, Cancer Res. 79 (18) (2019) 4612–4626.
[61] X. Han, M. Li, J. Xu, J. Fu, X. Wang, J. Wang, T. Xia, S. Wang, G. Ma, miR-1275 targets MDK/AKT signaling to inhibit breast cancer chemoresistance by lessening the properties of cancer stem cells, Int. J. Biol. Sci. 19 (1) (2023).
[62] N. Jiang, C. Zou, Y. Zhu, Y. Luo, L. Chen, Y. Lei, K. Tang, Y. Sun, W. Zhang, S. Li, Q. He, J. Zhou, Y. Chen, J. Luo, W. Jiang, Z. Ke, HIF-1α-regulated miR-1275 maintains stem cell-like phenotypes and promotes the progression of LUAD by simultaneously activating Wnt/β-catenin and Notch signaling, Theranostics 10 (6) (2020) 2553–2570.
[63] X. Tao, Y. Li, S. Fan, L. Wu, J. Xin, Y. Su, X. Xian, Y. Huang, R. Huang, W. Fang, Z. Liu, Downregulation of Linc00173 increases BCL2 mRNA stability via the miR-1275/PROCA1/ZFP36L2 axis and induces acquired cisplatin resistance of lung adenocarcinoma, J. Exp. Clin. Cancer Res. 42 (1) (2023) 12.
[64] T. Jiang, H. You, D. You, L. Zhang, M. Ding, B. Yang, A miR-1275 mimic protects myocardiocyte apoptosis by regulating the Wnt/NF-κB pathway in a rat model of myocardial ischemia-reperfusion-induced myocardial injury, Mol. Cell. Biochem. 466 (1–2) (2020) 129–137.
[65] Q.-H. Tong, H.-Y. Hu, H. Chai, A.-B. Wu, X.-H. Guo, S. Wang, Y.-F. Zhang, X.-Y. Fan, Dysregulation of the miR-1275/HK2 Axis contributes to the progression of hypoxia/reoxygenation-induced myocardial injury, Arch. Med. Res. 52 (5) (2021) 461–470.